
Article:
Domenico, D., Destra, P., Ricciardi, G. et al. (2019) Novel fluid inerter based tuned mass dampers for optimised structural control of base-isolated buildings. Journal of The Franklin Institute, 356 (14). pp. 7626-7649. ISSN: 0016-0032

https://doi.org/10.1016/j.jfranklin.2018.11.012

Novel fluid inerter based tuned mass dampers for optimised structural control of base-isolated buildings

Dario De Domenico[1*], Predaricka Deastra[2], Giuseppe Ricciardi[1], Neil D. Sims[2], David J.Wagg[2]

[1] Department of Engineering, University of Messina, Contrada Di Dio, 98166 Sant'Agata, Messina, Italy
[2] Department of Mechanical Engineering, University of Sheffield, Mappin Street, Sheffield S1 3JD, UK

* Corresponding author: Dario De Domenico, University of Messina. Email: dario.dedomenico@unime.it

ABSTRACT

This work studies the advantageous features of the fluid inerter device for optimised structural control of buildings. Experimental data are first presented to characterise the fluid inerter dynamics, and validate the simplified analytical formulations. Building on these observations, the device is modelled as an inerter in parallel with a nonlinear dashpot representing a power law damping term. The latter dissipative effects are mainly induced by the pressure drops occurring in helical channels due to the fluid viscosity and density. Then, novel passive vibration control schemes are implemented for the earthquake protection of base-isolated buildings by combining the fluid inerter with a tuned mass damper system. To account for the uncertain nature of the earthquake input, the base acceleration is modelled as a Kanai-Tajimi filtered stationary random process. The optimal fluid inerter parameters, namely inertance and damping, are identified numerically by minimising stochastic performance indices relevant to displacement, acceleration, and energy-based measures of the structural response. The nonlinear damping behaviour of the fluid inerter is fully incorporated in the optimal design procedure via the statistical linearization technique. Nonlinear response history analysis under an ensemble of 44 natural earthquake ground motions is carried out to assess the seismic performance of the system. Since inertance and damping are coupled characteristics in a real fluid inerter, design guidelines are finally outlined to determine the actual geometrical and mechanical properties of the device to achieve targeted parameters resulting from the optimisation procedure.

KEY WORDS: Fluid inerter; Earthquake protection; Structural control; Tuned mass damper; Base isolation; Optimal design.

1. INTRODUCTION

Since the Smith's [1] pioneering contribution in 2002, the inerter has become a popular mechanical device studied and used in different fields, from improved suspension systems in automotive engineering [2]-[6], to steering compensators for high-performance motorcycles [7], suspensions in railway engineering [8]-[10], mitigation of liquid sloshing in storage tanks [11], vibration suppression of optical tables [12] and even aircrafts landing gears [13].

The inerter can be usefully employed for the passive vibration control of civil engineering structures, particularly in structural dynamics applications [14], [15]. Furthermore, the beneficial mass amplification effect of the inerter can improve the seismic performance of conventional tuned mass damper (TMD) systems, thereby promoting the development of more effective vibration absorbers for earthquake engineering applications. Lower-mass and more effective alternatives to the traditional TMD can be developed through the inerter, namely the tuned mass damper inerter (TMDI) [16]-[19] and the tuned inerter damper (TID) [20]-[24]: in the first case the inertance replaces the TMD mass partly, instead in the second case it entirely substitutes the TMD mass.

Typical realizations of the inerter employ rack-and-pinion mechanisms [1], ball screw mechanisms [25], electromagnetic devices [26], and hydraulic devices [27]. The helical fluid inerter dealt with in this paper belongs to the latter class and was recently patented by Smith and collaborators [28], [29]. However, hydraulic engine mounts exploit the same inertial effect using rotating fluid, and were developed much earlier [30]. Specifically, the design of these mounts was based on the lever arm model of the Dynamic Anti-resonant Vibration Isolator (DAVI) concept, first patented in 1967 by Flannelly [31], which is also an inerter. More recent studies of the application of these mounts can be found in [32]-[34]. Devices that exploit relative acceleration to produce inertial force for civil engineering applications were also being

developed as modifications to viscous dampers in the late 1990s – see the tuned viscous mass damper (TVMD) described in [35] and references therein.

In certain circumstances, the hydraulic mechanism underlying the fluid inerter offers certain advantages over both the flywheel-based and mechanical ball screw inerter devices: for instance, it may reduce ratcheting, backlash and friction phenomena that are more pronounced in mechanical devices [36]. Additionally, one more advantageous feature of the fluid inerter is related to its inherent damping that results from the pressure drops occurring in helical channels due to the fluid viscosity and density.

The recent literature on the fluid inerter has mainly focused on the identification and modelling of this device based on some available experiments [27], [37]-[41]. Nevertheless, to the authors' best knowledge, with regard to the implementation of the fluid inerter in civil engineering applications to date there are just a couple of preliminary studies [42], [43], although we note that the TVMD described in [35] is a hybrid between fluid and mechanical inerter, the inertance being provided by a mechanical flywheel. Thus, while the rack-and-pinion inerter and the ball-screw inerter were extensively studied in several structural control layouts, see for example [44]-[48] along with the recent overview in [49], the more specific application of the fluid inerter to structural control of buildings is still at a preliminary stage of research, which has motivated the present research work.

1.1. Goal of the paper and research significance

The goal of this paper is to investigate the advantageous features of the fluid inerter in earthquake engineering applications, for optimised structural control of base-isolated (BI) buildings. The motivation for this study is related to some drawbacks typically suffered from BI buildings, mainly the large displacements concentrated at the isolation level (that may be an issue for the risk of pounding) and the vulnerability to long-period ground motions [50]. These

shortcomings were partly overcome through some hybrid control strategies, by placing a TMD below the isolation floor of the building [51], [52], see in this regard the recent practical case study in [53]. More effective structural control systems can be obtained by coupling the inerter with the TMD [54]. Thus, to complete the previous research work [19], we here expand the investigation by considering the fluid inerter in place of the rack-and-pinion inerter in such an enhanced structural control layout. Building on previous design methods [27] and some experimental observations [38], the fluid inerter is modelled as an inerter in parallel with a nonlinear dashpot representing a power law damping term for the fluid damping. Following this, novel passive vibration control schemes are studied via different combinations of the fluid inerter in conjunction with vibration absorbers. The optimal parameters of the fluid inerter, namely inertance and nonlinear damping, are identified numerically through the minimization of specific objective functions arising from the stochastic dynamic analysis of the system, by modelling the earthquake-induced acceleration as a random process. The nonlinear damping features of the fluid inerter are incorporated in the optimal design procedure through the statistical linearization technique. Then, the seismic performance is assessed via nonlinear response history analysis (RHA) under an ensemble of 44 earthquake ground motions. Strategies to simultaneously convert the targeted inertance and damping parameters resulting from the above optimisation procedure, which are two coupled terms in a real fluid inerter, into actual geometrical and mechanical properties of the device are finally discussed.

2. HELICAL FLUID INERTER MODELLING

The working principle of the helical fluid inerter was described in [27], [28] and is here briefly recalled for completeness and supplemented by some additional experimental observations [38]. The sketch of the device is shown in Figure 1, while the symbol nomenclature is listed in Table 1. The device consists of a piston moving within a cylinder that

contains a fluid. When the piston moves from one side to the other, it forces the fluid to flow through a helical coil. This flow generates an inertial force due to the moving fluid mass. A part of the resistive force is proportional to the relative acceleration between the two terminals of the device, that is

$$F_{\text{inertance}} \approx \left[\frac{m_{hel}}{1+\left(h/2\pi r_4\right)^2} \left(\frac{A_1}{A_2} \right)^2 \right] \ddot{x} = b\ddot{x} \tag{1}$$

where the *b* constant, representing the term within square brackets, has the dimensions of mass [kg] and is called inertance, and *x* denotes the relative displacement of the terminals.

The inertance is related to the mass of liquid in the helical channel $m_{hel} \approx \rho_f \ell A_2$. From Eq. (1) it is noted that the *b* value can be adjusted by simply scaling the ratio A_1 / A_2 (piston area to channel area), and this makes it potentially possible to achieve large inertance values with simple geometrical considerations. However, we note that (i) Eq. (1) is an idealised formula based on very simple assumptions and (ii) damping and inertance are coupled (via the geometry) and cannot be designed independently from one another as better clarified next.

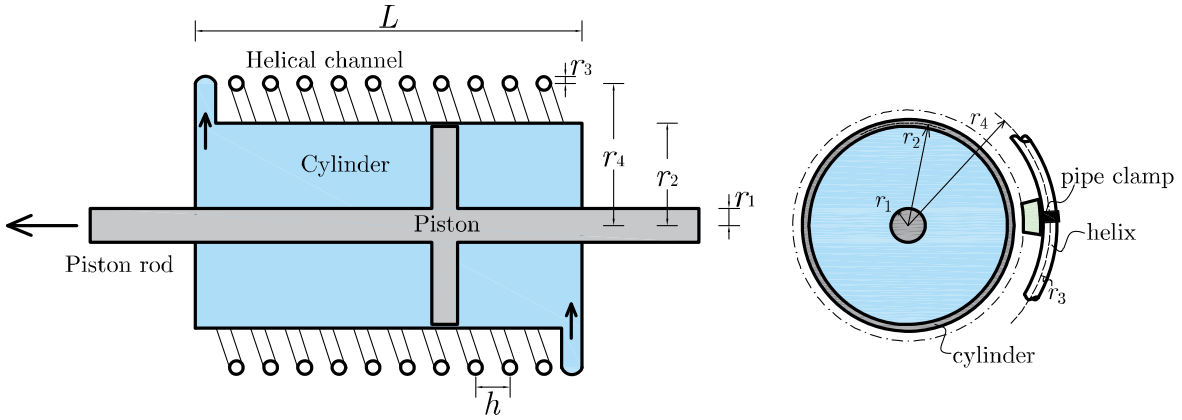

Figure 1 Schematic of the helical fluid inerter: longitudinal section (left); cross section (right)

Table 1 Nomenclature for geometrical dimensions and physical properties of the helical fluid inerter

Symbol [units]	Meaning
r_1 [m]	Radius of the piston
r_2 [m]	Inner radius of the cylinder
r_3 [m]	Inner radius of the helical channel
r_4 [m]	Radius of the helix
h [m]	Pitch of the helix
n_t [-]	Number of turns in the helix
L [m]	Inner length of the cylinder
$\ell = n_t\sqrt{h^2+(2\pi r_4)^2}$ [m]	Length of the helical channel
R_b [m]	Bend radius of the helical channel
$A_1 = \pi(r_2^2 - r_1^2)$ [m^2]	Cross-sectional area of the cylinder
$A_2 = \pi r_3^2$ [m^2]	Cross-sectional area of the helical channel
ν_f [cSt]	Kinematic viscosity of the fluid at reference temperature
μ_f [Pa s][1]	Dynamic viscosity of the fluid at reference temperature
ρ_f [kg/m^3]	Mass density of the fluid at reference temperature

[1] the dynamic viscosity in [cSt] and the dynamic viscosity in [Pa s] are related to each other through the mass density expressed in [kg/m^3] according to $\mu_f = \rho_f \times \nu_f \times 10^{-6}$

The ideal inerter would only have its force proportional to relative acceleration. As said above, some deviations from the ideal behaviour caused by friction, backlash etc. can be minimised in the fluid inerter device as compared to mechanical alternatives. There are, however, other nonlinear damping contributions to the total resistive force of the fluid inerter that cause deviations from the ideal behaviour in Eq. (1) for large piston velocities. These dissipative effects are related to the intrinsic viscosity of the fluid inducing pressure drops that cannot be eliminated as they are part of the working principle of this hydraulic device. Thus, these nonlinear damping contributions should be incorporated in a proper modelling of the fluid inerter. Among these contributions, the most important term is related to the pressure drop $\Delta p_{\text{helical}}$ due to the viscous effects in the helical channel. Some simplified modelling assumptions can be introduced in this regard. According to Darcy's formula for turbulent conditions, for a smooth pipe such pressure drop is expressed as [28]

$$\Delta p_{\text{helical}} = \frac{1}{r_3^2} 0.079\,\text{Re}^{-0.25}\,\rho_f v_f^2 \tag{2}$$

wherein v_f is the mean velocity of the fluid in the helical channel, which can be related to the piston velocity $\dot{x}$ through the volume conservation law $v_f = \dot{x} A_1 / A_2$, and $\mathrm{Re} = \rho_f v_f 2r_3 / \mu_f$ is the Reynolds number. From Eq. (2), the damping force to maintain a steady velocity is

$$F_{d-\mathrm{helical}} = \Delta p_{\mathrm{helical}} A_1 = \frac{0.0664 \mu_f^{0.25} \rho_f^{0.75} \ell A_1}{r_3^{1.25}} \left(\frac{A_1}{A_2} \right)^{1.75} \dot{x}^{1.75} = c_{\mathrm{f}1} \dot{x}^{1.75} \tag{3}$$

where $c_{\mathrm{f}1}$ is a coefficient that depends on physical properties of the fluid and the geometry of the device. A slightly different formulation was proposed in [27] where other effects like the secondary flow due to the centrifugal force in the curved helical channel were considered

$$F_{d-\mathrm{helical2}} = \Delta p_{\mathrm{helical2}} A_1 = 0.03426 \frac{2\rho_f \ell A_1}{\sqrt{2r_3 R_b}} \left(\frac{A_1}{A_2} \right)^2 \dot{x}^2 + 17.54 \frac{2\mu_f \ell A_1}{(2r_3)^2} \left(\frac{A_1}{A_2} \right) \dot{x} = c_{\mathrm{f}2} \dot{x}^2 + c_{\mathrm{f}3} \dot{x} \tag{4}$$

which consists of a linear term plus a squared term whose coefficients $c_{\mathrm{f}2}, c_{\mathrm{f}3}$ depend on the physical and geometrical properties of the fluid inerter. The two formulations in Eqns. (3) and (4) for the helical tube damping force lead to rather different values for high velocities. In particular, the formulation of Eq. (4), which accounts for the secondary flow effects due to channel curvatures, overestimates the damping force as compared to Eq. (3), which instead explicitly incorporates turbulent flow conditions but based on an underlying straight pipe assumption. We do not claim that either of these two formulations should be considered as definitive, or as superior over the other, but they are included here and presented alongside one another so that they may be applied in the appropriate modelling circumstance.

Other small energy losses occur at either end of the channel (inlet and outlet), where flow transition between the main cylinder and the narrow channel occurs; other effects are due to friction at the side of the piston. These forces, $F_{d-\mathrm{inlet}}$, $F_{d-\mathrm{outlet}}$ and F_{shear}, respectively, can be approximated using the expressions reported by Swift et al. [27]. The summation of all the force contributions generates the total resisting force of the fluid inerter device as

$$F_{\text{total}} = F_{\text{inertance}} + F_{d-\text{helical}} + (F_{d-\text{inlet}} + F_{d-\text{outlet}}) + F_{\text{shear}} = F_{\text{inertance}} + F_{d-\text{total}}$$
$$= \left[\frac{m_{hel}}{1+\left(h/2\pi r_4\right)^2} \left(\frac{A_1}{A_2} \right)^2 \right] \ddot{x} + \left[\frac{0.0664 \mu_f^{0.25} \rho_f^{0.75} \ell A_1}{r_3^{1.25}} \left(\frac{A_1}{A_2} \right)^{1.75} \dot{x}^{1.75} + 0.75 A_1 \rho_f \left(\frac{A_1}{A_2} \right)^2 \dot{x}^2 + \frac{\mu_f 2\pi r_2 L}{\Delta r} \dot{x} \right] \quad (5)$$

from which we note that the force consists of a part $F_{\text{inertance}}$ proportional to the relative acceleration (related to the ideal inerter) and another part $F_{d-\text{total}}$, dependent on the relative velocity, induced by the parasitic damping caused by the pressure drops and fluid friction losses.

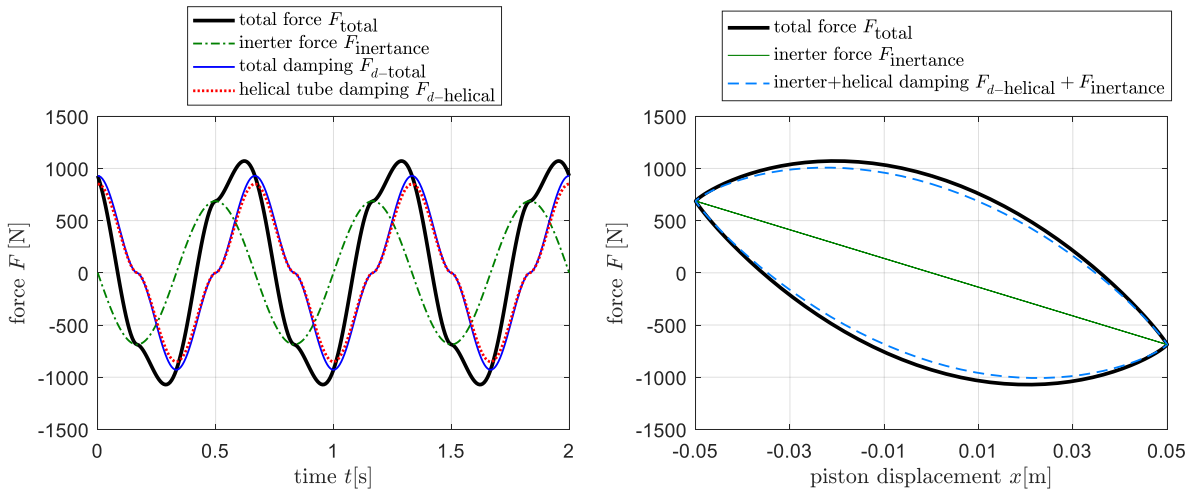

Figure 2 Force time histories (left) and hysteretic loops (right) of the fluid inerter described in [28] subject to a sinusoidal displacement input with frequency 1.5Hz and amplitude 50mm

In an attempt to present the hysteretic characteristics of a fluid inerter device, in Figure 2 the force time histories and the corresponding force-displacement loops are shown for the fluid inerter parameters described in the patent document [28] subject to a sinusoidal displacement input with frequency 1.5Hz and amplitude 50mm. It is noted that the hysteretic characteristics of this idealised device are well captured by only considering the sum of the helical tube damping and the inertance force, i.e., $F_{\text{total}} \approx F_{\text{inertance}} + F_{d-\text{helical}}$. This suggests that a simplified model of the fluid inerter could well be justified for many applications. This simplified model would incorporate an ideal inerter in parallel with a nonlinear dashpot representing the parasitic damping (viscosity-related) effects via a power law damping term, as shown schematically in

Figure 3. Throughout this paper the first modelling assumption for the pressure drops $F_{d-\text{helical}}$ as per Eq. (3) is adopted, with a power law damping in the form $c_p^{\text{NL}}\dot{x}^{\alpha}$ with $\alpha = 1.75$ according to the patent formula [28].

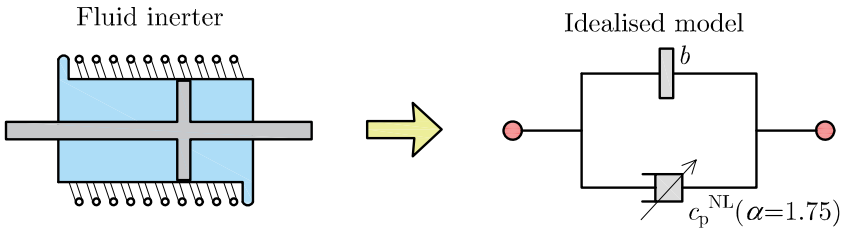

Figure 3 Simplified model of fluid inerter through an inerter in parallel with a nonlinear dashpot representing a power law damping term (inerter + parasitic damping)

It is worth noting that all the expressions proposed for the evaluation of the pressure drops due to the fluid viscosity were for steady flow with no end effects. Nevertheless, in a real fluid inerter device the flow will be unsteady, oscillatory and subject to end effects. One immediate issue is that, due to reversals in velocity during oscillations, the flow velocity will be crossing the transition between laminar and turbulent multiple times during every cycle. This means that all the above relationships, valid for steady flow in a straight pipe, should be interpreted as preliminary approximations of the more complex behaviour of the fluid inerter, which requires more sophisticated computational tools than just a single, simplified analytical formula.

2.1. Some additional considerations from experiments

In this subsection, some experimental results from [38] are compared with the analytical result using Eq. (5). The main parameters of the fluid inerter prototype are listed in Table 2, while other details of the experimental setup were reported in [38] and are here omitted for brevity. Assuming the total force is the sum of inertial and damping force in parallel, the comparison of analytical and experimental total force time histories is given in Figure 4 for a typical sinusoidal excitation. The amplitude of the predicted total force is 400N but in the experiment this is 1000N. Closer inspection of the time history, and consideration of the

damper design, suggests that the forces in the experiment are strongly influenced by friction, which was neglected in the simulation. To fit the experimental force amplitude, a friction force of $F_{\text{friction}} = f\,\text{sgn}(\dot{x})$ is included, where f=550N and ẋ is relative velocity between the piston ends. Including this friction force provides a close fit between experimental force and simulation, as seen in Figure 4.

Table 2 Geometrical and physical parameters of the tested fluid inerter device

Symbol [units]	Value
r_1 [m]	0.014
r_2 [m]	0.025
r_2 [m]	0.006
r_4 [m]	0.120
h [m]	0.030
n_t [-]	7
ρ_f [kg/m^3]	802
μ_f [Pa s]	0.00168

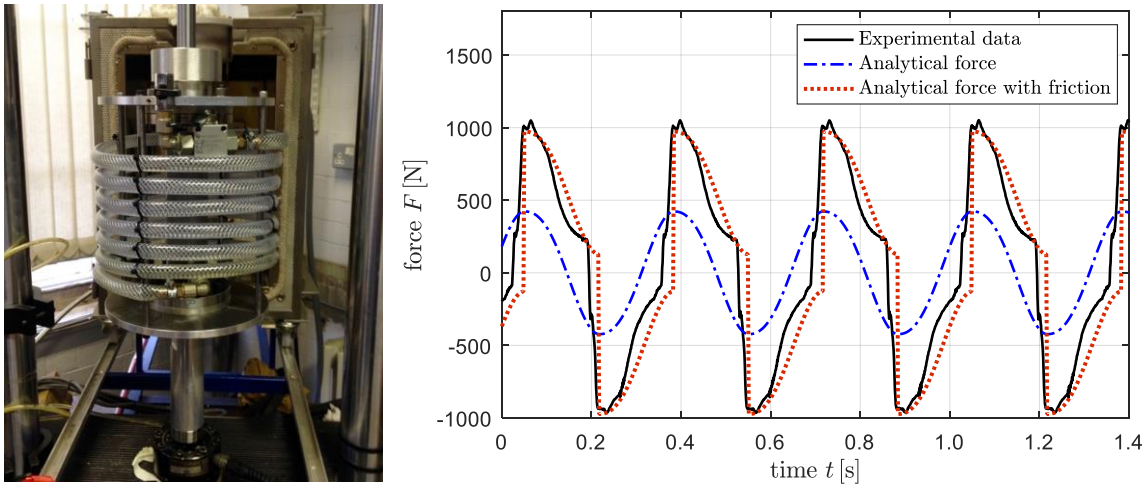

Figure 4 Analytical vs experimental force (sinusoidal excitation, amplitude 17.5mm, frequency 3Hz)

In this regard, Shen *et al.* [39] suggested that this friction force could be associated with the interaction between the piston and cylinder of the fluid inerter. The prototype used in the present study [38] also had significant friction from the piston shaft seals. However, Shen *et al.* [39] reported that the friction force becomes less significant at higher excitation frequencies, and when the relative motion is higher. In general, the friction force is reduced with the

increasing of force and relative velocity between the piston ends (i.e. the Stribeck effect). In earthquake engineering applications, it is expected that the force being applied to the device is very large (hundreds of kN as confirmed in the below numerical examples and design considerations later on in this paper). Consequently, in earthquake engineering applications it is expected that friction contributions in the range of 0.5-1 kN can be neglected in the preliminary sizing and optimisation of the device design, and that the simplified model sketched in Figure 3 of inerter in parallel with nonlinear dashpot can be resorted to.

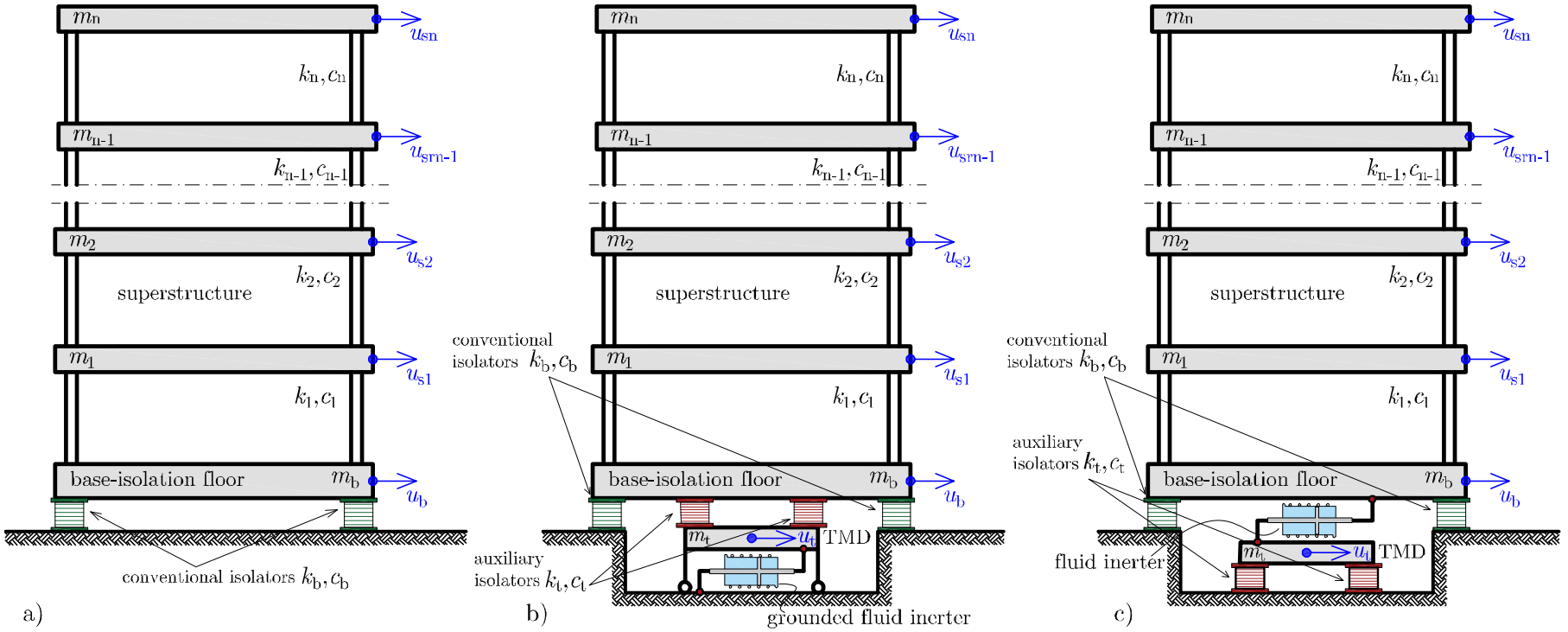

Figure 5 Sketch of the structural systems analysed: a) base-isolated (BI) building; b) BI building with TMD and grounded fluid-inerter, also termed TMDI with parasitic damping (TMDI-PD); c) BI building with fluid-inerter-based TMD (FIB-TMD)

3. NOVEL FLUID INERTER BASED TMD SYSTEMS FOR BASE-ISOLATED BUILDINGS

In this section some novel fluid-inerter-based TMD systems are introduced to improve the structural control of BI buildings. Reference is made to the simple sketches illustrated in Figure 5 where a shear-type planar model of *n*-story BI building is assumed, having mass lumped at each floor. The mass, damping and stiffness matrix of the superstructure (in its fixed-base configuration) are denoted as $\mathbf{M}_\mathrm{s}, \mathbf{C}_\mathrm{s}, \mathbf{K}_\mathrm{s}$ respectively. The base isolators are featured by a strong nonlinear behaviour that may be dependent upon velocity, temperature, and axial force in a very intricate manner [55]. Nevertheless, in a preliminary model the base-isolation system can be modelled as an additional single-degree-of-freedom (SDOF) system through its linear effective stiffness and equivalent viscous damping characteristics $k_\mathrm{b}, c_\mathrm{b}$ that can be determined from real-scale experiments as described in [56]. The basement mass is denoted as m_b.

The multi-degree-of-freedom (MDOF) systems shown in Figure 5 include a TMD at basement in conjunction with the fluid inerter device and, thus, complete the previous overview in [49] where, instead, only rack-and-pinion (flywheel-based) inerter devices were considered for the analysis of simple SDOF structural systems. In line with the nomenclature adopted in [19], for a better comprehension of the structural systems the spring and damping properties of the TMD system $k_\mathrm{t}, c_\mathrm{t}$ are associated with an auxiliary set of isolators that are introduced in addition to the above conventional isolators (featured by $k_\mathrm{b}, c_\mathrm{b}$). From a structural dynamics viewpoint, the fluid inerter is easily incorporated in the equations of motion via the simplified model displayed in Figure 3. Two different configurations are presented in Figure 5 depending on the fluid inerter placement: 1) a grounded fluid inerter gives rise to a so-called TMDI with parasitic damping (TMDI-PD), which is an enhanced variant of the TMDI first presented in [16] with an additional power law damping term due to the fluid damping; 2) a so-called fluid-

inerter-based TMD (FIB-TMD) system in which the fluid inerter is located in between the TMD mass and the base-isolation floor, which, apart from the nonlinearity of the damping behaviour of the device, shows some similarities to a model proposed by Saitoh in a different context [46]. These two dynamic layouts are just two examples of suspension configurations incorporating the fluid inerter based on two structural control systems earlier proposed in the literature. However, many other schemes might be developed, which is beyond the main scope of the present paper. These two systems have N=n+2 DOFs, represented by the n displacements of the superstructure stories $\mathbf{u}_{\mathrm{s}} = [u_{\mathrm{s}1}, \ldots, u_{\mathrm{s}n}]^T$, the displacement of the conventional isolators u_{b} and that of the TMD u_{t}, all meant relative to the ground. For convenience, it is useful to introduce the displacements of the superstructure relative to the base-isolation floor $\mathbf{u}_{\mathrm{sr}} = \mathbf{u}_{\mathrm{s}} - \boldsymbol{\tau}_{\mathrm{s}}\, u_{\mathrm{b}}$ with $\boldsymbol{\tau}_{\mathrm{s}}$ a $n \times 1$ vector of ones. The equations of motions for the two systems subject to a horizontal ground motion acceleration $\ddot{u}_{\mathrm{g}}$ at their base, and are presented separately in the following subsection. Only the horizontal earthquake-induced excitation has been considered for simplicity, while analysis of the vertical excitation certainly deserves further investigation as proposed by Lu et al. [57].

3.1. Governing equations of motion

Applying the D'Alembert's principle to the TMDI-PD system in Figure 5b) leads to:

$$\begin{aligned} &\mathbf{M}_{\mathrm{s}}\ddot{\mathbf{u}}_{\mathrm{sr}} + \mathbf{C}_{\mathrm{s}}\dot{\mathbf{u}}_{\mathrm{sr}} + \mathbf{K}_{\mathrm{s}}\mathbf{u}_{\mathrm{sr}} = -\mathbf{M}_{\mathrm{s}}\boldsymbol{\tau}_{\mathrm{s}}\left(\ddot{u}_{\mathrm{g}} + \ddot{u}_{\mathrm{b}}\right) \\ &m_{\mathrm{b}}\ddot{u}_{\mathrm{b}} + c_{\mathrm{b}}\dot{u}_{\mathrm{b}} + k_{\mathrm{b}}u_{\mathrm{b}} - f_{\mathrm{s1,b}} - f_{\text{aux-iso1}} = -m_{\mathrm{b}}\ddot{u}_{\mathrm{g}} \\ &m_{\mathrm{t}}\ddot{u}_{\mathrm{t}} + f_{\text{aux-iso1}} + f_{\mathrm{FI1}} = -m_{\mathrm{t}}\ddot{u}_{\mathrm{g}} \end{aligned} \tag{6}$$

where $f_{\mathrm{s1,b}} = c_{\mathrm{1}}\dot{u}_{\mathrm{sr1}} + k_{\mathrm{1}}u_{\mathrm{sr1}}$ is the force transmitted from the first floor of the superstructure to the base-isolation floor, $f_{\text{aux-iso1}} = c_{\mathrm{t}}\dot{u}_{\mathrm{tbr}} + k_{\mathrm{t}}u_{\mathrm{tbr}}$ (with $u_{\mathrm{tbr}} = u_{\mathrm{t}} - u_{\mathrm{b}}$ denoting the displacement of the TMD relative to the base-isolation system) is the force transmitted from the TMD to the

base-isolation floor through the auxiliary isolators, and $f_{\mathrm{FI1}} = b\ddot{u}_{\mathrm{t}} + c_p^{NL}\left|\dot{u}_{\mathrm{t}}\right|^{1.75}\mathrm{sgn}(\dot{u}_{\mathrm{t}})$ is the nonlinear resistive force of the fluid inerter that is grounded in this configuration, where $\mathrm{sgn}(\cdot)$ is the signum function. Introducing the signum function in the correct definition of the power law damping term is useful to prevent inconsistencies for negative velocities. Thus, the fluid inerter force depends upon the acceleration $\ddot{u}_{\mathrm{t}}$ and the velocity $\dot{u}_{\mathrm{t}}$ relative to the ground.

Applying the D'Alembert's principle to the FIB-TMD system in Figure 5c) leads to:

$$\begin{aligned}
&\mathbf{M}_{\mathrm{s}}\ddot{\mathbf{u}}_{\mathrm{sr}} + \mathbf{C}_{\mathrm{s}}\dot{\mathbf{u}}_{\mathrm{sr}} + \mathbf{K}_{\mathrm{s}}\mathbf{u}_{\mathrm{sr}} = -\mathbf{M}_{\mathrm{s}}\boldsymbol{\tau}_{\mathrm{s}}\left(\ddot{u}_{\mathrm{g}} + \ddot{u}_{\mathrm{b}}\right)\\
&m_{\mathrm{b}}\ddot{u}_{\mathrm{b}} + c_{\mathrm{b}}\dot{u}_{\mathrm{b}} + k_{\mathrm{b}}u_{\mathrm{b}} - f_{\mathrm{s1,b}} - f_{\mathrm{FI2}} = -m_{\mathrm{b}}\ddot{u}_{\mathrm{g}}\\
&m_{\mathrm{t}}\ddot{u}_{\mathrm{t}} + f_{\text{aux-iso2}} + f_{\mathrm{FI2}} = -m_{\mathrm{t}}\ddot{u}_{\mathrm{g}}
\end{aligned} \tag{7}$$

where in this case the force of the auxiliary isolators is $f_{\text{aux-iso2}} = c_{\mathrm{t}}\dot{u}_{\mathrm{t}} + k_{\mathrm{t}}\dot{u}_{\mathrm{t}}$, whereas the nonlinear resistive force of the fluid inerter, placed in between the TMD and the base-isolation floor, assumes the shape $f_{\mathrm{FI2}} = b\ddot{u}_{\mathrm{tbr}} + c_p^{NL}\left|\dot{u}_{\mathrm{tbr}}\right|^{1.75}\mathrm{sgn}(\dot{u}_{\mathrm{tbr}})$, thus depending upon the relative acceleration and velocity between TMD and base-isolation system.

3.2. Earthquake ground motion representation

The seismic input is affected by a large degree of uncertainty in space, size, time and attenuation. Modelling this with deterministic approaches, for instance via harmonic excitations, cannot take into account the intrinsic random nature of the real problem. A simplified way to consider some aspects of the stochastic nature of the seismic excitation is to model the earthquake-induced base acceleration $\ddot{u}_{\mathrm{g}}$ as the realization of a stationary zero-mean Gaussian random process. The effects of transient phenomena induced by more accurate models of non-stationary stochastic excitations were investigated in the relevant literature for both SDOF [58] and MDOF systems [59] with inerters. In order to incorporate the frequency content of the earthquake excitation, the Kanai-Tajimi power spectral density (PSD) function

is assumed in this paper, with a second filter in series as proposed by Clough and Penzien [60] to eliminate the inconsistencies observed in the vanishing frequency regime:

$$S_{\ddot{u}_g}(\omega) = \frac{\omega_g^4 + 4\zeta_g^2\omega_g^2\omega^2}{\left(\omega_g^2 - \omega^2\right)^2 + 4\zeta_g^2\omega_g^2\omega^2} \frac{\omega^4}{\left(\omega_f^2 - \omega^2\right)^2 + 4\zeta_f^2\omega_f^2\omega^2} S_w \tag{8}$$

where $\omega_g, \zeta_g, \omega_f, \zeta_f$ are filter parameters that influence the frequency content and can be related to the engineering site (e.g., soil characteristics [61]), while the white-noise intensity level S_w is related to the bedrock peak ground acceleration (PGA) $\ddot{u}_{g0}$ by the formula

$$S_w = \frac{0.141\zeta_g \ddot{u}_{g0}^2}{\omega_g\sqrt{1+4\zeta_g^2}}. \tag{9}$$

3.3. Stochastic response through the statistical linearization technique (SLT)

Since the equations of motion (6) and (7) contain nonlinear terms induced by the fluid inerter power law damping, linear random vibration theory is not applicable to determine the stochastic response of the system. One of the most effective tools to deal with nonlinearities in the stochastic dynamic analysis framework is the statistical linearization technique (SLT) [62]. The SLT enables the replacement of the nonlinear power law damping terms entering the differential equations of motion with equivalent linear viscous damping ones as follows

$$c_p^{NL}\left|\dot{x}\right|^{1.75}\operatorname{sgn}(\dot{x}) \quad \underset{\text{after SLT}}{\rightarrow} \quad c_{p,\text{eq}}\dot{x} \quad (\dot{x} = \dot{u}_t \text{ in TMDI-PD; } \dot{x} = \dot{u}_{tbr} \text{ in FIB-TMD}) \tag{10}$$

which implies the introduction of a linearization coefficient $c_{p,\text{eq}}$. This coefficient is defined so as to be "equivalent", in statistical sense, to the nonlinear damping coefficient c_p^{NL}. Indeed, it is determined by minimising, in a mean-square sense, the error/difference between the nonlinear and linearized damping force, which yields [62]

$$c_{p,\mathrm{eq}} = c_p^{NL} \frac{E[|\dot{x}|^{2.75}]}{E[\dot{x}^2]} \tag{11}$$

where $E[\cdot]$ denotes the expectation operator. To compute the expected value of the above terms in Eq. (11), one should know the probability density function (PDF) of the system response beforehand, which is obviously an unknown at this stage. Thus, a reasonable assumption for the PDF $p_{\dot{x}}(\dot{x})$ should be introduced a priori to explicitly determine the linearization coefficient $c_{p,\mathrm{eq}}$ in (11). For a zero-mean Gaussian excitation and linear behaviour of the system, $p_{\dot{x}}(\dot{x})$ would be zero-mean Gaussian too by virtue of the Central Limit Theorem. This is also rather acceptable for the nonlinear system at hand, although it is not exactly true as the power law damping terms produce a non-Gaussian response process even if the seismic excitation is Gaussian [62]. Avoiding more complicated non-Gaussian variants of the SLT that are beyond the scope of the present paper [63], the classical Gaussian SLT is here resorted to, which results in the following expression for the linearization coefficient in (11)

$$c_{p,\mathrm{eq}} = c_p^{NL} \frac{2^{1.375}\Gamma(1.875)}{\sqrt{\pi}} \sigma_{\dot{x}}^{0.75} = 1.3952\, c_p^{NL} \sigma_{\dot{x}}^{0.75} \tag{12}$$

where $\Gamma(\cdot)$ is the gamma function and $\sigma_{\dot{x}}$ is the standard deviation of $\dot{x}$. Since $\sigma_{\dot{x}}$ is unknown and is inherently related to $c_{p,\mathrm{eq}}$, the determination of $c_{p,\mathrm{eq}}$ is performed iteratively, exploiting input-output relationships in the frequency domain [62] until convergence is met.

Once the differential equations of motion (6) and (7) are linearized through the SLT, they can be re-written in the following matrix-vector compact form

$$\mathbf{M}\ddot{\mathbf{u}}(t) + \mathbf{C}\dot{\mathbf{u}}(t) + \mathbf{K}\mathbf{u}(t) = -\boldsymbol{\tau}\ddot{u}_g(t) \tag{13}$$

with $\mathbf{u}(t)^T = [\mathbf{u}_{\mathrm{sr}}, u_{\mathrm{b}}, u_{\mathrm{t}}]$ the displacements vector, $\boldsymbol{\tau}^T = [\mathbf{M}_{\mathrm{s}}\boldsymbol{\tau}_{\mathrm{s}}, M_{\mathrm{tot}}, m_{\mathrm{t}}]$, with $M_{\mathrm{tot}} = M_{\mathrm{s,tot}} + m_{\mathrm{b}}$ the total mass of the BI building and $M_{\mathrm{s,tot}} = \boldsymbol{\tau}_{\mathrm{s}}^T \mathbf{M}_{\mathrm{s}} \boldsymbol{\tau}_{\mathrm{s}}$ the superstructure

mass, while the overall mass, damping and stiffness matrices in the TMDI-PD system are

$$\mathbf{M}=\begin{bmatrix} \mathbf{M}_{\mathrm{s}} & \mathbf{M}_{\mathrm{s}}\boldsymbol{\tau}_{\mathrm{s}} & \mathbf{0} \\ \boldsymbol{\tau}_{\mathrm{s}}^{T}\mathbf{M}_{\mathrm{s}} & M_{\mathrm{tot}} & 0 \\ \mathbf{0}^{T} & 0 & m_{\mathrm{t}}+b \end{bmatrix};\ \mathbf{C}=\begin{bmatrix} \mathbf{C}_{\mathrm{s}} & \mathbf{0} & \mathbf{0} \\ \mathbf{0}^{T} & c_{\mathrm{b}}+c_{\mathrm{t}} & -c_{\mathrm{t}} \\ \mathbf{0}^{T} & -c_{\mathrm{t}} & c_{\mathrm{t}}+c_{p,\mathrm{eq}} \end{bmatrix};\ \mathbf{K}=\begin{bmatrix} \mathbf{K}_{\mathrm{s}} & \mathbf{0} & \mathbf{0} \\ \mathbf{0}^{T} & k_{\mathrm{b}}+k_{\mathrm{t}} & -k_{\mathrm{t}} \\ \mathbf{0}^{T} & -k_{\mathrm{t}} & k_{\mathrm{t}} \end{bmatrix} \tag{14}$$

and the corresponding matrices in the FIB-TMD system are

$$\mathbf{M}=\begin{bmatrix} \mathbf{M}_{\mathrm{s}} & \mathbf{M}_{\mathrm{s}}\boldsymbol{\tau}_{\mathrm{s}} & \mathbf{0} \\ \boldsymbol{\tau}_{\mathrm{s}}^{T}\mathbf{M}_{\mathrm{s}} & M_{\mathrm{tot}}+b & -b \\ \mathbf{0}^{T} & -b & m_{\mathrm{t}}+b \end{bmatrix};\ \mathbf{C}=\begin{bmatrix} \mathbf{C}_{\mathrm{s}} & \mathbf{0} & \mathbf{0} \\ \mathbf{0}^{T} & c_{\mathrm{b}}+c_{p,\mathrm{eq}} & -c_{p,\mathrm{eq}} \\ \mathbf{0}^{T} & -c_{p,\mathrm{eq}} & c_{\mathrm{t}}+c_{p,\mathrm{eq}} \end{bmatrix};\ \mathbf{K}=\begin{bmatrix} \mathbf{K}_{\mathrm{s}} & \mathbf{0} & \mathbf{0} \\ \mathbf{0}^{T} & k_{\mathrm{b}} & 0 \\ \mathbf{0}^{T} & 0 & k_{\mathrm{t}} \end{bmatrix}. \tag{15}$$

From Eq. (13), the random vibration theory produces the following set of covariance matrices (collecting the mean square response quantities under a zero-mean stochastic seismic input) of the displacement, velocity and absolute acceleration response of the system

$$\begin{aligned} \boldsymbol{\Sigma}_{\mathbf{uu}} &= \mathrm{E}[\mathbf{u}\mathbf{u}^{T}]=\int_{-\infty}^{\infty}\mathbf{H}_{\mathrm{U}}(\omega)\mathrm{S}_{\ddot{u}_{\mathrm{g}}}(\omega)\mathbf{H}_{\mathrm{U}}(\omega)^{*T}\mathrm{d}\omega \\ \boldsymbol{\Sigma}_{\dot{\mathbf{u}}\dot{\mathbf{u}}} &= \mathrm{E}[\dot{\mathbf{u}}\dot{\mathbf{u}}^{T}]=\int_{-\infty}^{\infty}\omega^{2}\mathbf{H}_{\mathrm{U}}(\omega)\mathrm{S}_{\ddot{u}_{\mathrm{g}}}(\omega)\mathbf{H}_{\mathrm{U}}(\omega)^{*T}\mathrm{d}\omega \\ \boldsymbol{\Sigma}_{\ddot{\mathbf{u}}_{\mathrm{A}}\ddot{\mathbf{u}}_{\mathrm{A}}} &= \mathrm{E}[\ddot{\mathbf{u}}_{\mathrm{A}}\ddot{\mathbf{u}}_{\mathrm{A}}^{T}]=\int_{-\infty}^{\infty}\mathbf{H}_{\ddot{\mathrm{U}}_{\mathrm{A}}}(\omega)\mathrm{S}_{\ddot{u}_{\mathrm{g}}}(\omega)\mathbf{H}_{\ddot{\mathrm{U}}_{\mathrm{A}}}(\omega)^{*T}\mathrm{d}\omega \end{aligned} \tag{16}$$

in which $(\cdot)^{*T}$ is the complex conjugate transpose. $\mathbf{H}_{\mathrm{U}}(\omega)$ is the system displacement transfer function vector such that $\mathbf{U}(\omega)=\mathbf{H}_{\mathrm{U}}(\omega)\ddot{U}_{\mathrm{g}}(\omega)$, with $\mathbf{U}(\omega)$ and $\ddot{U}_{\mathrm{g}}(\omega)$ denoting the Fourier transform of $\mathbf{u}(t)$ and $\ddot{u}_{g}(t)$, respectively, and $\mathbf{H}_{\ddot{\mathrm{U}}_{\mathrm{A}}}(\omega)$ is the corresponding transfer function vector of the absolute accelerations $\ddot{\mathbf{u}}_{\mathrm{A}}(t)$, such that $\ddot{\mathbf{U}}_{\mathrm{A}}(\omega)=\mathbf{H}_{\ddot{\mathrm{U}}_{\mathrm{A}}}(\omega)\ddot{U}_{\mathrm{g}}(\omega)$. Based on Eq. (13), the vectors $\mathbf{H}_{\mathrm{U}}(\omega)$ and $\mathbf{H}_{\ddot{\mathrm{U}}_{\mathrm{A}}}(\omega)$ have the following shape, respectively

$$\begin{aligned} &\mathbf{H}_{\mathrm{U}}(\omega)=-\left[-\omega^{2}\mathbf{M}+\mathrm{i}\omega\mathbf{C}+\mathbf{K}\right]^{-1}\boldsymbol{\tau} \\ &\mathbf{H}_{\ddot{\mathrm{U}}_{\mathrm{A}}}(\omega)=\left[-\omega^{2}\mathbf{A}\mathbf{H}_{\mathrm{U}}(\omega)+\boldsymbol{\tau}\right] \quad \text{with} \quad \mathbf{A}=\begin{bmatrix} \mathbf{I}_{n} & \boldsymbol{\tau}_{\mathrm{s}} & 0 \\ 0 & 1 & 0 \\ 0 & 0 & 1 \end{bmatrix} \end{aligned} \tag{17}$$

where $\mathrm{i}=\sqrt{-1}$ is the imaginary unit, $\mathbf{I}_n$ the identity matrix of order n, and the matrix $\mathbf{A}$ is such that $\ddot{\mathbf{u}}_{\mathrm{A}}(t)=\mathbf{A}\ddot{\mathbf{u}}(t)+\boldsymbol{\tau}\ddot{u}_g(t)$ and has been introduced because of the difference between $\mathbf{u}_{\mathrm{sr}}$ (relative to the base-isolation floor) and $\mathbf{u}_{\mathrm{s}}$ (relative to the ground). All the response statistics are defined by the matrices in (16) that, as said above, depend upon the linearization coefficient $c_{p,\mathrm{eq}}$ and, thus, can be determined through an iterative numerical procedure [62].

4. OPTIMAL DESIGN OF THE FLUID INERTER

The fluid inerter device can be optimally designed by minimising an objective function viewed as a representative indicator of the system response. Considering the stochastic nature of the earthquake excitation, a set of so-called stochastic performance indices (SPIs) are introduced in this paper on the basis of elements of the covariance matrices of the system response presented in the previous section. This is in line with other studies from the relevant literature dealing with SDOF systems equipped with inerter-based devices [64], [65].

For a given BI building, for a given TMD mass and a given set of auxiliary isolators of the TMD, and for a given earthquake probabilistic characterisation in terms of frequency content and intensity as described by the PSD function (8), the goal is to find the best parameters b and c_p^{NL} of the fluid inerter device (according to the modelling assumption sketched in Figure 3) that minimise a selected SPI. The PSD function (8) is defined by $\omega_{\mathrm{g}}=15\,\mathrm{rad/s}$, $\zeta_{\mathrm{g}}=0.6$, $\omega_{\mathrm{f}}=1.5\,\mathrm{rad/s}$, $\zeta_{\mathrm{f}}=0.6$, PGA $\ddot{u}_{\mathrm{g0}}=0.3\,\mathrm{g}$ (g denoting the acceleration of gravity), which may be associated with firm soil conditions [61]. To obtain a preliminary estimate of the system response in the optimal design procedure, we assume that the superstructure vibrates in its first (fixed-base) mode. Consequently, the building is described by the dynamic characteristics of the fundamental mode of vibration, namely natural frequency ω_{s}, damping ratio ζ_{s}, and effective modal mass m_{s}, the latter being assumed coincident with the total mass of the

building $m_{\mathrm{s}} \approx M_{\mathrm{s,tot}}$. The base-isolation system is characterised by natural frequency $\omega_{\mathrm{b}} = \sqrt{k_{\mathrm{b}} / M_{\mathrm{tot}}}$ and damping ratio $\zeta_{\mathrm{b}} = c_{\mathrm{b}} / 2M_{\mathrm{tot}}\omega_{\mathrm{b}}$. To account for the distribution of the mass in the BI building, a mass ratio $\mu_{\mathrm{s}} = M_{\mathrm{s,tot}} / M_{\mathrm{tot}} < 1$ is introduced. The mass ratio characterising the TMD is $\mu_{\mathrm{t}} = m_{\mathrm{t}} / M_{\mathrm{tot}}$. Based on Eq. (16), the corresponding covariance matrices of this simplified 3-DOF system are

$$\mathbf{\Sigma_{uu}} = \begin{bmatrix} \sigma_{u_{\mathrm{sr}}}^2 & \sigma_{u_{\mathrm{sr}}u_{\mathrm{b}}} & \sigma_{u_{\mathrm{sr}}u_{\mathrm{t}}} \\ \sigma_{u_{\mathrm{sr}}u_{\mathrm{b}}} & \sigma_{u_{\mathrm{b}}}^2 & \sigma_{u_{\mathrm{b}}u_{\mathrm{t}}} \\ \sigma_{u_{\mathrm{sr}}u_{\mathrm{t}}} & \sigma_{u_{\mathrm{b}}u_{\mathrm{t}}} & \sigma_{u_{\mathrm{t}}}^2 \end{bmatrix}; \mathbf{\Sigma_{\dot{u}\dot{u}}} = \begin{bmatrix} \sigma_{\dot{u}_{\mathrm{sr}}}^2 & \sigma_{\dot{u}_{\mathrm{sr}}\dot{u}_{\mathrm{b}}} & \sigma_{\dot{u}_{\mathrm{sr}}\dot{u}_{\mathrm{t}}} \\ \sigma_{\dot{u}_{\mathrm{sr}}\dot{u}_{\mathrm{b}}} & \sigma_{\dot{u}_{\mathrm{b}}}^2 & \sigma_{\dot{u}_{\mathrm{b}}\dot{u}_{\mathrm{t}}} \\ \sigma_{\dot{u}_{\mathrm{sr}}\dot{u}_{\mathrm{t}}} & \sigma_{\dot{u}_{\mathrm{b}}\dot{u}_{\mathrm{t}}} & \sigma_{\dot{u}_{\mathrm{t}}}^2 \end{bmatrix}; \mathbf{\Sigma_{\ddot{u}_{\mathrm{A}}\ddot{u}_{\mathrm{A}}}} = \begin{bmatrix} \sigma_{\ddot{u}_{\mathrm{srA}}}^2 & \sigma_{\ddot{u}_{\mathrm{srA}}\ddot{u}_{\mathrm{bA}}} & \sigma_{\ddot{u}_{\mathrm{srA}}\ddot{u}_{\mathrm{tA}}} \\ \sigma_{\ddot{u}_{\mathrm{srA}}\ddot{u}_{\mathrm{bA}}} & \sigma_{\ddot{u}_{\mathrm{bA}}}^2 & \sigma_{\ddot{u}_{\mathrm{bA}}\ddot{u}_{\mathrm{tA}}} \\ \sigma_{\ddot{u}_{\mathrm{srA}}\ddot{u}_{\mathrm{tA}}} & \sigma_{\ddot{u}_{\mathrm{bA}}\ddot{u}_{\mathrm{tA}}} & \sigma_{\ddot{u}_{\mathrm{tA}}}^2 \end{bmatrix}. \quad (18)$$

A five-story building is considered with fundamental period $T_{\mathrm{s}} = 2\pi / \omega_{\mathrm{s}} = 0.5\,\mathrm{s}$, and damping ratio $\zeta_{\mathrm{s}} = 0.02$, while the mass at each floor is assumed constant and coincident with the underlying basement mass m_{b}, so that the mass ratio $\mu_{\mathrm{s}} = 5/6$. This building is seismically isolated at its base. The conventional isolators of the base-isolation system are assumed as low-damping rubber bearings with effective damping ratio $\zeta_{\mathrm{b}} = 0.1$ and natural period $T_{\mathrm{b}} = 2\pi / \omega_{\mathrm{b}} = 3\,\mathrm{s}$. The auxiliary isolators of the TMD, associated with a reasonable mass ratio $\mu_{\mathrm{t}} = 0.1$, are varied within a wide parametric study, by examining a family of stiffness ratios $\kappa = k_{\mathrm{t}} / \mathrm{k}_{\mathrm{b}}$, and dissipation ratios $\chi = c_{\mathrm{t}} / c_{\mathrm{b}}$ in order to identify the range of optimal characteristics that achieve the best structural control. For each combination of parameters, the optimal inertance ratio $\beta = b / M_{\mathrm{tot}}$, related to the apparent mass produced by the fluid inerter device, and the optimal dissipation ratio $\xi = c_p^{NL} / c_{\mathrm{b}}$ (or $\xi_{\mathrm{eq}} = c_{p,\mathrm{eq}} / c_{\mathrm{b}}$), related to the nonlinear power law damping term of the fluid damping, are identified numerically via the minimisation of a selected SPI. In mathematical terms, this turns out to be a nonlinear multi-variable single-objective constrained optimisation problem

$$\min_{\boldsymbol{\theta}} \mathrm{SPI}(\boldsymbol{\theta}) \quad \text{such that } \boldsymbol{\theta}_{\mathrm{lb}} \le \boldsymbol{\theta} \le \boldsymbol{\theta}_{\mathrm{ub}} \tag{19}$$

where $\boldsymbol{\theta} = [\beta, \xi]$ is the vector of fluid inerter design variables and $\boldsymbol{\theta}_{\mathrm{lb}}$ and $\boldsymbol{\theta}_{\mathrm{ub}}$ denote possible lower and upper bound vectors introduced to ensure a physically consistent solution (for example, $\boldsymbol{\theta}_{\mathrm{lb}} = [0, 0]$ guarantees positive β and ξ coefficients).

Four different SPIs are analysed for an overall structural control of both the BI building and the TMD system. The first SPI represents the displacement demand of the BI building, assumed as the displacement variance of the structure

$$\mathrm{SPI}_1 = \sigma^2_{u_{\mathrm{s}}} / \sigma^2_{u_{\mathrm{s0}}} \quad \text{displacement performance index} \tag{20}$$

where $\sigma^2_{u_{\mathrm{s}}} = \sigma^2_{u_{\mathrm{sr}}} + \sigma^2_{u_{\mathrm{b}}} + 2\sigma_{u_{\mathrm{sr}}u_{\mathrm{b}}}$. The SPI_1 is presented in a dimensionless format, normalised by the corresponding variance in the BI building without TMD $\sigma^2_{u_{\mathrm{s0}}}$, in order to clearly assess the beneficial effects induced by the fluid inerter based TMD system (values $\mathrm{SPI}_1 < 1$ indicate performance improvement as compared to the uncontrolled BI building). The second SPI represents the variance of the total acceleration of the structure

$$\mathrm{SPI}_2 = \sigma^2_{\ddot{u}_{\mathrm{As}}} / \sigma^2_{\ddot{u}_{\mathrm{As0}}} \quad \text{acceleration performance index} \tag{21}$$

where $\ddot{u}_{\mathrm{As}} = \ddot{u}_{\mathrm{sr}} + \ddot{u}_{\mathrm{b}} + \ddot{u}_{\mathrm{g}}$ and $\sigma^2_{\ddot{u}_{\mathrm{As}}} = E[\ddot{u}^2_{\mathrm{As}}] = 4\zeta^2_{\mathrm{s}}\omega^2_{\mathrm{s}}\sigma^2_{\dot{u}_{\mathrm{sr}}} + \omega^4_{\mathrm{s}}\sigma^2_{u_{\mathrm{sr}}}$. The SPI_2 is also presented in a dimensionless format, normalised by the corresponding variance in the uncontrolled BI building $\sigma^2_{\ddot{u}_{\mathrm{As0}}}$. Additionally, in [19] an energy-based SPI called filtered energy index (FEI) was introduced to assess the effectiveness of the TMDI structural control system from the perspective of the equation of relative energy balance. The FEI represents the portion of the global seismic input energy that is not dissipated by the TMD system and, thus, penetrates into the BI building. As a result, this SPI is a useful indicator of the overall structural performance. Without going into details of the derivations for brevity, following the same rationale explained

in [19] for the FEI definition, but adapted here to the novel equations of motion of this paper, the FEI for the TMDI-PD and for the FIB-TMD has the following expressions, respectively

$$\mathrm{SPI}_3 = \begin{cases} 1 - \dfrac{2\zeta_\mathrm{b}\omega_\mathrm{b}(\chi\sigma^2_{\dot{u}_\mathrm{tbr}} + \xi_\mathrm{eq}\sigma^2_{\dot{u}_\mathrm{t}})}{2\zeta_\mathrm{s}\omega_\mathrm{s}\mu_\mathrm{s}\sigma^2_{\dot{u}_\mathrm{sr}} + 2\zeta_\mathrm{b}\omega_\mathrm{b}(\sigma^2_{\dot{u}_\mathrm{b}} + \chi\sigma^2_{\dot{u}_\mathrm{tbr}} + \xi_\mathrm{eq}\sigma^2_{\dot{u}_\mathrm{t}})} & \text{TMDI-PD} \\ 1 - \dfrac{2\zeta_\mathrm{b}\omega_\mathrm{b}(\chi\sigma^2_{\dot{u}_\mathrm{t}} + \xi_\mathrm{eq}\sigma^2_{\dot{u}_\mathrm{tbr}})}{2\zeta_\mathrm{s}\omega_\mathrm{s}\mu_\mathrm{s}\sigma^2_{\dot{u}_\mathrm{sr}} + 2\zeta_\mathrm{b}\omega_\mathrm{b}(\sigma^2_{\dot{u}_\mathrm{b}} + \chi\sigma^2_{\dot{u}_\mathrm{tbr}} + \xi_\mathrm{eq}\sigma^2_{\dot{u}_\mathrm{t}})} & \text{FIB-TMD} \end{cases} \quad \text{filtered energy index} \quad (22)$$

where $\sigma^2_{\dot{u}_\mathrm{tbr}} = \sigma^2_{\dot{u}_\mathrm{t}} + \sigma^2_{\dot{u}_\mathrm{b}} - 2\sigma_{\dot{u}_\mathrm{b}\dot{u}_\mathrm{t}}$. It is noted that the FEI (SPI_3) is a dimensionless quantity: it assumes a unitary value for the system without TMD ($\chi = \xi_\mathrm{eq} = 0$), and decreases with increasing dissipation capability of the vibration absorber. Finally, the fourth and last SPI is related to the displacement demand of the TMD system, which should not become disproportionately large in order to ensure feasibility and cost-effectiveness of the TMD implementation in practical cases

$$\mathrm{SPI}_4 = \sigma^2_{u_\mathrm{tbr}} / \sigma^2_{u_\mathrm{b0}} \quad \text{TMD stroke index} \quad (23)$$

where $\sigma^2_{u_\mathrm{tbr}} = \sigma^2_{u_\mathrm{t}} + \sigma^2_{u_\mathrm{b}} - 2\sigma_{u_\mathrm{b}u_\mathrm{t}}$. The SPI_4 is related to the stroke of the TMD and, in line with the previous indicators, is presented in a dimensionless format, normalised by the displacement variance of the base-isolation system in the uncontrolled configuration $\sigma^2_{u_\mathrm{b0}}$.

In Figure 6 the optimal design parameters of the fluid inerter $(\beta_\mathrm{opt}, \xi_\mathrm{opt})$ of the TMDI-PD system that minimise the SPI_1 are reported along with the performance evaluation of the optimised system through the four SPIs introduced above. Analogous results are shown in Figure 7 for the FIB-TMD system. By careful inspection of the reported graphs the following general remarks can be drawn:

i) the optimal inertance ratio β_opt is not particularly sensitive to variations of the stiffness ratio κ of the auxiliary isolators, but is moderately affected by the dissipation ratio χ

as it increases with increasing χ in the range [0.1-2];

ii) in an opposite manner, the optimal dissipation ratio ξ_{opt} is strongly influenced by the stiffness ratio κ as it increases with increasing κ in the range [0.3-1.2], but is not particularly affected by the dissipation ratio χ of the auxiliary isolators;

iii) the stiffness ratio κ has a different impact on the considered response indicators, as the displacement demand and the energy-based indicators SPI_1, SPI_3 and SPI_4 decrease with increasing κ, but the acceleration index SPI_2 slightly increase with increasing κ in the range [0.4-1.2];

iv) increasing the damping features of the auxiliary isolators will always lead to improvements of the overall structural control of the BI building, as all the considered SPIs decrease with increasing χ;

v) both the optimal fluid inerter optimal parameters (β_{opt}, ξ_{opt}) are slightly higher for the TMDI-PD system than for the FIB-TMD;

vi) for equal parameters of the auxiliary isolators (κ, χ), the performance of the TMDI-PD system is better than that of the FIB-TMD system except for the TMD stroke, as the response indicators SPI_1-SPI_3 are lower in the TMDI-PD case than in the FIB-TMD case of 10-30% but SPI_4 is higher.

From the above general remarks, it emerges that an optimal design strategy to improve the structural control of BI building is based on the TMDI-PD system with the following parameters: $\chi = 2$, $\kappa = 0.8$, $\beta_{opt} \approx 1.5$, $\xi_{opt} \approx 6$. Indeed, this combination of parameters results in values of the SPIs well below the unity, meaning an effective vibration reduction as compared to the BI building. If the displacement demand of the secondary (TMD-related) mass is also of major importance, the FIB-TMD system would be preferable to the TMDI-PD system provided a slight degradation of the system performance can be accepted.

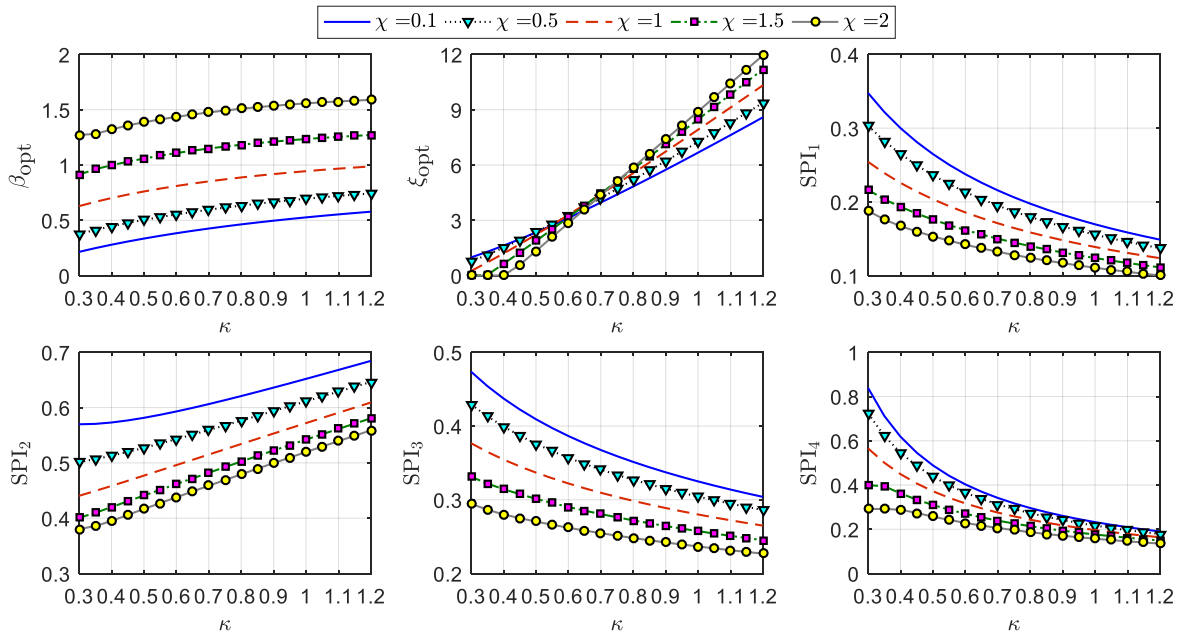

Figure 6 Optimal fluid inerter design graphs and performance evaluation: BI building with TMDI-PD ($\kappa = k_t / k_b$, $\chi = c_t / c_b$ represent the stiffness and damping ratio of the TMD)

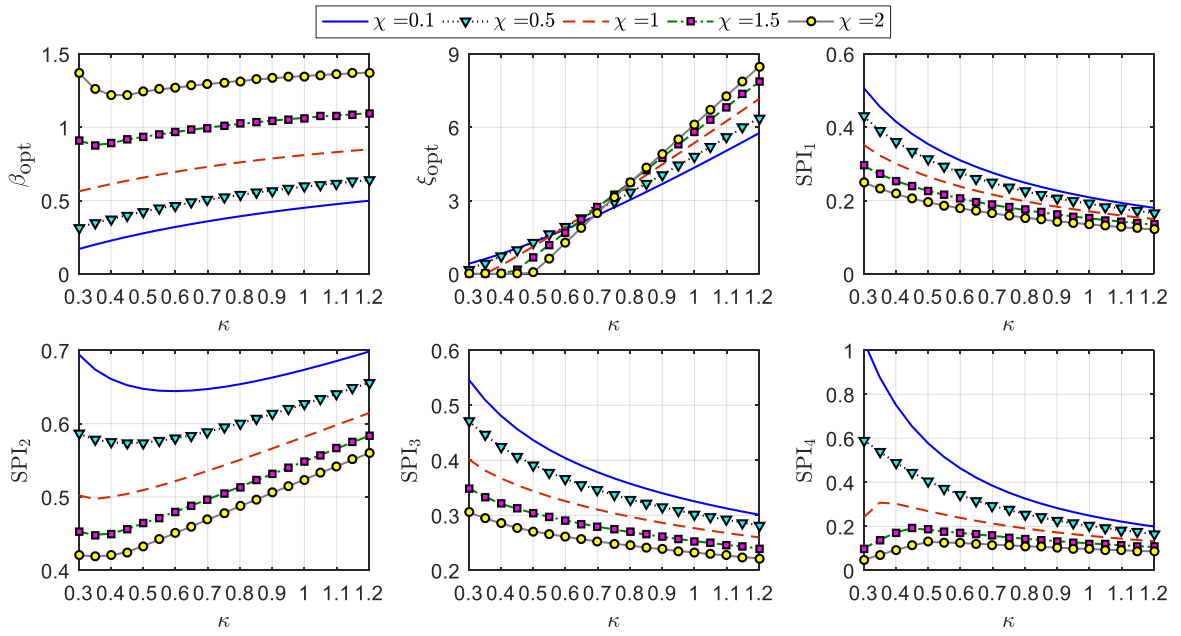

Figure 7 Optimal fluid inerter design graphs and performance evaluation: BI building with FIB-TMD ($\kappa = k_t / k_b$, $\chi = c_t / c_b$ represent the stiffness and damping ratio of the TMD)

5. NONLINEAR RESPONSE HISTORY ANALYSIS AND SEISMIC PERFORMANCE

The seismic performance of the proposed fluid inerter based tuned mass damper systems

when applied to BI buildings is here investigated via nonlinear RHA. A shear-type model of a five-story structure with uniform mass $m = 50000\text{kg}$ for each story, and uniform stiffness $k = 97\text{MN/m}$ is considered, which results in a fundamental natural period of the superstructure $T_\text{s} = 2\pi / \omega_\text{s} = 0.5\,\text{s}$. The damping matrix $\mathbf{C}_\text{s}$ is assumed such that the modal damping ratio ζ_s is equal to 0.02 for all the vibration modes of the building. The basement mass is assumed as $m_\text{b} = 50000\text{kg}$. The above data lead to $M_\text{tot} = 300000\text{kg}$ and $\mu_\text{s} = 5/6$. The conventional isolators of the base-isolation system are low-damping rubber bearings with $\zeta_\text{b} = 0.1$ and natural period $T_\text{b} = 2\pi / \omega_\text{b} = 3\text{s}$, which corresponds to effective lateral stiffness of the isolation floor $k_\text{b} = 1.3159\text{MN/m}$. The TMD mass ratio is assumed as $\mu_\text{t} = 0.1$ and the auxiliary isolators have a slightly lower stiffness than the conventional ones, and medium-to-high damping characteristics: $\kappa = 0.8$ and $\chi = 2$. All these input data are purposely chosen to be consistent with the parameters adopted in Section 4 for the optimisation procedure. Therefore, the design graphs can be resorted to for the selection of the optimal fluid inerter parameters $(\beta_\text{opt}, \xi_\text{opt})$ that are specifically $(1.5079, 5.8709)$. Considering the above data, this results in $b = 452380[\text{kg}]$ and $c_p^{NL} = 737760[\text{N(s/m)}^{1.75}]$.

To consider a realistic earthquake input, an ensemble of 44 historically recorded ground motions belonging to the FEMA P695 far-field record set [66] has been assumed as seismic excitation at the base of the BI buildings. This is a benchmark set of ground motions widely adopted in the literature by various authors to investigate the behaviour of other TMD-like systems [67]. The ground motions components in the FEMA P695 are extracted from the PEER NGA database and are pertinent to site class C (soft rock/very dense soil) or D (stiff soil). This is consistent with the assumption of firm soil conditions in the Kanai-Tajimi PSD function (8) to develop the optimal design graphs in Figure 6 and Figure 7, on which the above-mentioned fluid inerter parameters are based. The RHA serves to validate the optimal design procedure

discussed in section 4 and to assess the actual seismic performance of the proposed structural control strategies for a realistic earthquake scenario characterised by non-stationary seismic input and including the nonlinearity of the fluid inerter device.

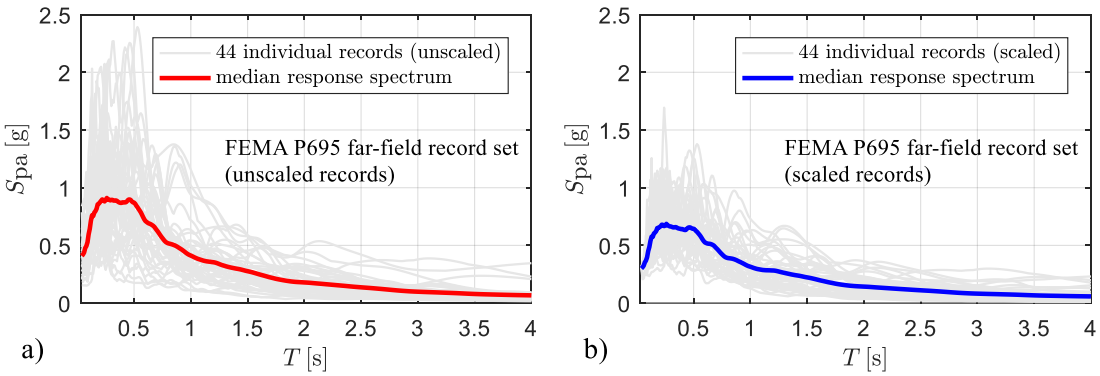

Figure 8 Pseudo-acceleration elastic response spectra for the 44 natural ground motions of the FEMA P695 far-field record set [66]: a) unscaled records; b) scaled records to a PGA=0.3 g

Considering the nonlinear character of the system response, it is important to assume a consistent intensity level for the earthquake excitation. Thus, the 44 individual ground motions, having a PGA ranging from 0.21 g to 0.82 g, have all been scaled to a common PGA of 0.3 g, in line with the assumption made in the optimal design procedure. The median response spectra of the unscaled and scaled records for a 0.05 damping ratio are reported in Figure 8. The time-history response is computed for each seismic event by direct integration of the nonlinear equations of motion (6) and (7) via a fourth-order Runge-Kutta algorithm. Then, the seismic performance is evaluated in statistical terms (in line with the probabilistic framework adopted for the seismic input) as average (on the 44 responses) absolute peak (MAX) and average root-mean-square (RMS) of a set of response indicators y_i calculated according to

$$\text{average MAX}(y_i) = \frac{1}{44}\sum_{j=1}^{44} \max_t \{y_i(t)\}; \quad \text{average RMS}(y_i) = \frac{1}{44}\sum_{j=1}^{44} \text{rms}_t \{y_i(t)\}. \tag{24}$$

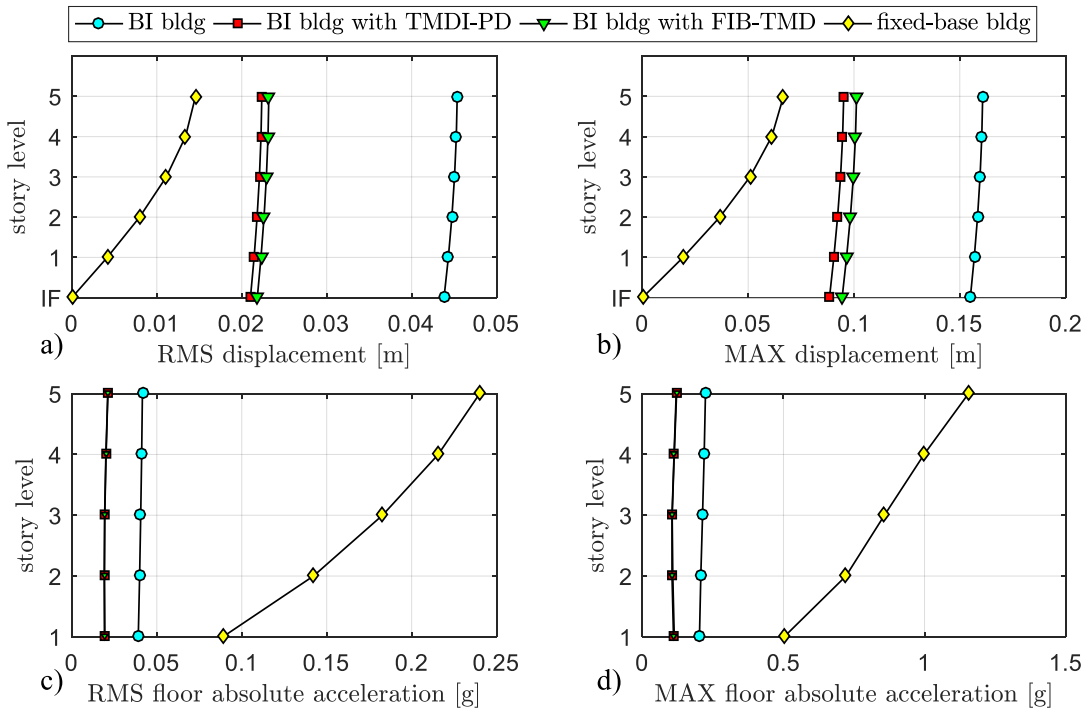

Figure 9 Seismic performance (in terms of average RMS and MAX values of displacement and floor absolute acceleration) of proposed fluid inerter based TMD systems compared to traditional BI building (without TMD) and fixed-base building under the FEMA P695 far-field record set

The seismic performance of the proposed fluid inerter based TMD systems in terms of average RMS and MAX values of displacement and floor absolute acceleration is illustrated in Figure 9. It is seen that both the TMDI-PD and FIB-TMD systems lead to a considerable reduction of the displacement demand (the acronym "IF" on the vertical axis denotes the "isolation floor") and also of the absolute floor acceleration (the latter is less evident because of the scale of the plot) in comparison with the BI building. The average reductions achieved by the TMDI-PD in terms of RMS and MAX values of the last-floor displacement (compared to the BI building) are 51% and 41%, respectively; those achieved by the FIB-TMD are 49% and 37%, respectively. The average reductions achieved by the TMDI-PD in terms of RMS and MAX values of the last-floor absolute acceleration (compared to the BI building) are 49% and 45%, respectively; those achieved by the FIB-TMD are 48% and 46%, respectively.

The performance of the fixed-base building is also illustrated in Figure 9 for comparative purposes: as expected, since the fixed-base building is stiffer than all the other base-isolated

configurations (with and without TMD), the displacement demand is lower, but the acceleration is considerably higher. This is consistent with the above-reported pseudo-acceleration response spectra. The performance of the TMDI-PD is slightly better than that of the FIB-TMD in terms of displacement reduction, but is rather comparable with regard to absolute floor accelerations. All these results are in reasonable agreement with the design graphs developed in section 4.

As an example of earthquake response, the time histories of the last-floor displacement u_{s5} and of the stroke of the isolators (u_{tbr} for the systems with TMD, u_b for the BI building without TMD) are reported in Figure 10. The results are pertinent to one (arbitrarily) selected ground motion among the 44 considered of the FEMA P695 record set, namely a component of the Imperial Valley 1979 seismic event. Results for other samples are qualitatively similar and are not reported for brevity. The displacement response is effectively damped by both the proposed fluid inerter based systems to a rather comparable extent for this ground motion, and the stroke is reduced more in the FIB-TMD system than in the TMDI-PD. This is consistent with the design graphs developed in section 4 and with the above discussions.

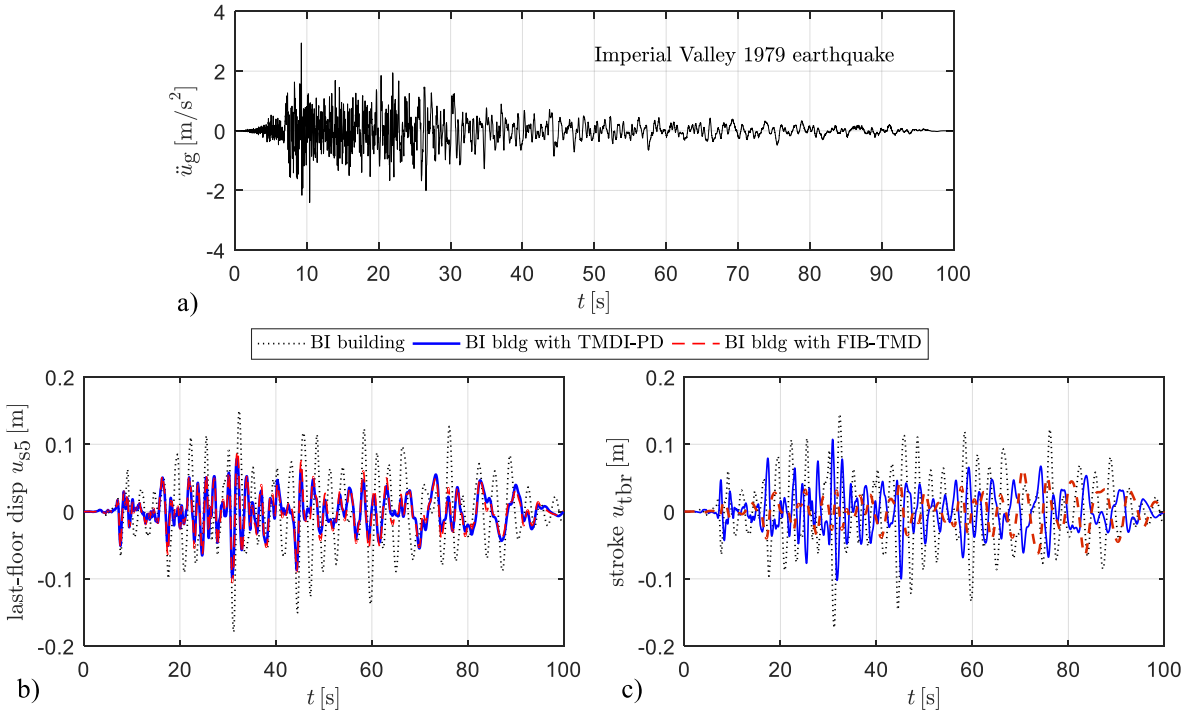

Figure 10 Time histories and structural control performance of proposed fluid inerter based TMD systems compared to traditional BI building (without TMD) for the Imperial Valley 1979 earthquake

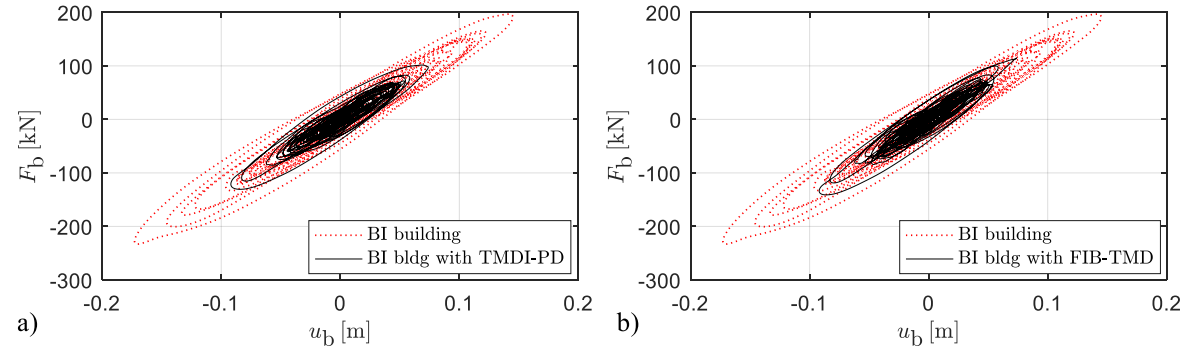

Figure 11 Comparison of hysteretic force-versus-displacement loops of seismic isolators in BI building with and without fluid inerter based TMD systems for Imperial Valley 1979 earthquake: a) TMDI-PD; b) FIB-TMD

Since the working principle of the TMD is to absorb the greatest amount of energy from the earthquake excitation, it is interesting to quantify the remaining amount of energy that needs to be dissipated by the BI building. This estimation is line with the definition of the FEI indicator introduced in section 4. The energy dissipated by the BI building is mainly concentrated at the isolation level, where the seismic isolators undergo large displacement and experience large hysteretic loops. The force-versus-displacement loops of the seismic isolators

corresponding to the Imperial Valley 1979 earthquake are depicted in Figure 11. It is seen that hysteretic loops corresponding to the systems with fluid inerter (either in the form of TMDI-PD or FIB-TMD) are considerably narrower than those of the BI building for the same ground motion acceleration. This confirms that, as anticipated above, part of the earthquake input energy is effectively dissipated by the TMD systems, and that the fluid inerter systems enable an improved structural control of the BI building. In principle, narrower hysteretic loops imply the potential use of smaller isolators. Thus, the possibility of adopting smaller isolation devices could compensate for the additional cost related to the implementation of the (slightly more involved) fluid inerter based TMD strategies proposed in this paper.

6. DESIGN CONSIDERATIONS ON COUPLED INERTANCE AND DAMPING

The goal of this section is to design the fluid inerter device used for the previous numerical examples, such that $b = 452380[\text{kg}]$ and $c_p^{NL} = 737760[\text{N(s/m)}^{1.75}]$. The design of fluid inerter dimensions involves coupled inertance and damping given in Eq. (1) and (3). Both equations are the function of seven parameters: $r_1, r_2, r_3, r_4, r_d, L, \rho_f, \mu_f$ where r_d is the space between the cylinder and the helical channel given by $r_d = r_4 - (r_2 + r_3)$. Previous works by the authors in [42] described an ad-hoc approach to choose these parameters, so that the fluid inerter achieves the targeted values of inertance and damping resulting from the optimisation procedure. The approach relied on the fact that the damping and inertance are insensitive to changes in some parameters. Consequently these parameters can be chosen based upon practical design considerations, so that the number of unknown parameters in Eq. (1) and (3) can be reduced. In this study, two parameters were selected as free variables: r_2 and r_3. This is because these two parameters were found to be the most sensitive to the changing of b and c_p^{NL} values. The other parameters were fixed to reasonable values given in Table 3.

Table 3 Fixed parameters of the fluid inerter device to design

Symbol [units]	Value
r_1 [m]	0.1
r_d [m]	0.06
L [m]	1.0
ρ_f [kg/m^3]	1000
μ_f [Pa s]	0.001

With reference to Table 3, the diameter of the piston r_1 must be large enough that the piston is strong enough to resist the stresses due to large forces being applied at the piston ends. Assuming, as a very extreme scenario, the maximum force at the maximum relative velocity between the piston ends of 1m/s is 5000kN, the stress at the piston ends is 159.15Mpa. Using steel (S355JR) with yield stress of 355Mpa for the piston material, this r_1 value is sufficient. In reality, the actual relative velocities experienced by the device are well below these extreme values: the average maximum velocity computed from the nonlinear RHA is around 0.4m/s, thus there is a large safety factor against collapse.

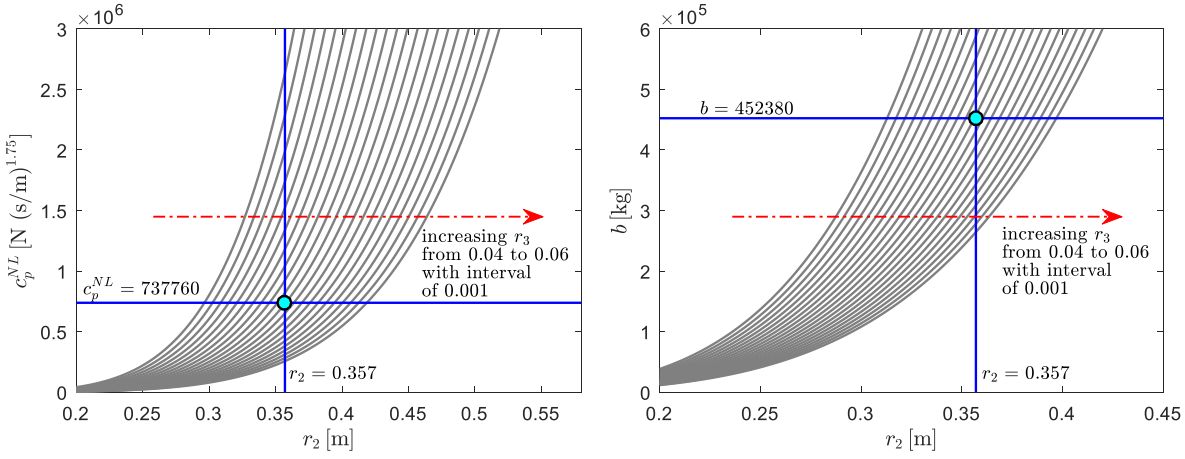

Figure 12 Design parameters identification via parametric approach: a) nonlinear damping coefficient vs r_2 for a family of r_3 curves; b) inertance vs r_2 for a family of r_3 curves

Fixing those parameters in Table 3, both Eq. (1) and (3) now can be written as functions of r_2 and r_3 only. The number of turns of the helical channel was set as a function of r_3 given by $n_t = (L - 2r_3)/2r_3$. The helical pitch h was assumed equal to $2r_3$. Having only two free

parameters, r_2 and r_3 now can be determined via an iteration process. Given the targeted optimum design parameters of $b = 452380[\text{kg}]$ and $c_p^{NL} = 737760[\text{N(s/m)}^{1.75}]$, the obtained values for r_2 and r_3 are 0.357m and 0.05m, respectively. Figure 12a) and b) show how the damping coefficient and inertance relate to r_2 and r_3, respectively. As can be seen from Figure 12, both the r_2 and r_3 parameters significantly affect the system performance. These two parameters are directly related to the dimensions of the fluid inerter device – inner radius of the cylinder and inner radius of the helical channel. As such, it is expected that these parameters can easily be realized in practical applications by current manufacturing skills. An earlier investigation of some of the authors of the present paper [42] has shown that the other geometrical parameters play a less important role in the definition of the targeted values of inertance and damping. It can be seen that $r_2 = 0.357$ intersect at line $r_3 = 0.05$ for the given optimum b and $c_p^{NL} c^{NL}$ values in both graphs. The actual b and c_p^{NL} values given from the actual dimensions of the fluid inerter are 457505kg and 729940 $\text{N(s/m)}^{1.75}$.

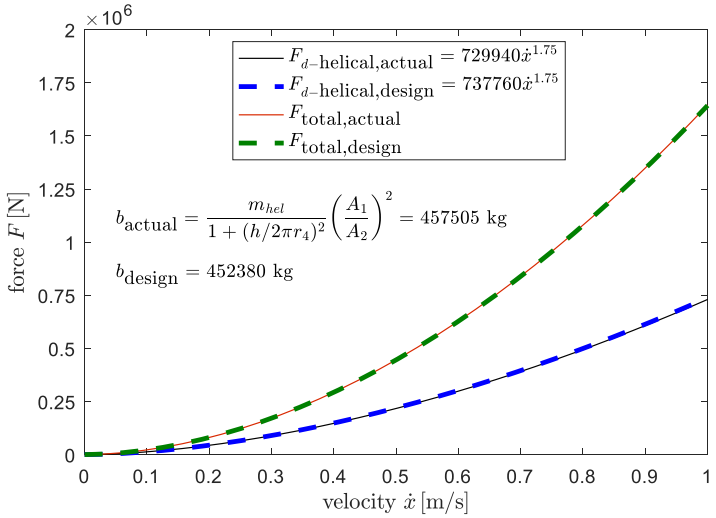

Figure 13 Force vs velocity curve for the fluid inerter with the design parameters compared to the optimal (target) parameters

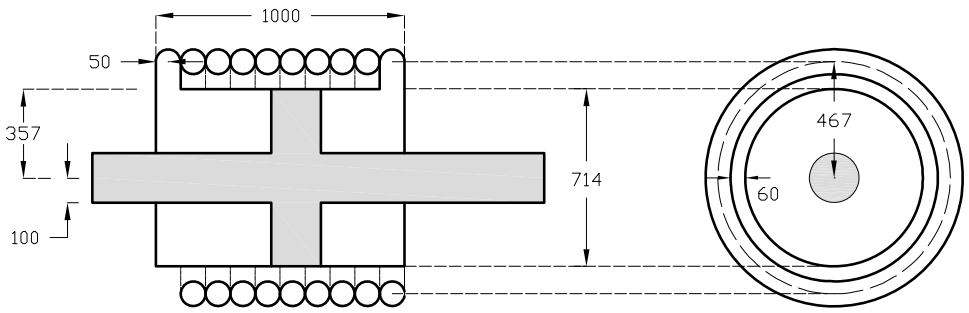

Figure 14 Fluid inerter dimensions based on the target parameters from the optimisation procedure (unit in mm)

Figure 13 compares the force-vs-velocity relationship between the design and actual values of the fluid inerter. Both total force and damping force from the actual fluid inerter are very close to the design specifications with percentage of errors around 1%. By inspection of the forces involved in the designed fluid inerter, it is evident that friction contributions in the range 0.5-1kN, which may be significant for lower forces and small velocity testing, can justifiably be neglected for earthquake engineering applications where the forces involved are much larger. A schematic design drawing with the assumed dimensions of the fluid inerter is displayed in Figure 14.

7. CONCLUDING REMARKS

The advantages of fluid inerters for optimised structural control of buildings have been investigated, with particular emphasis on earthquake loading. The helical fluid inerter presents some peculiar hysteretic characteristics as compared to the rack-and-pinion inerter and to the ball-screw inerter, which have been more widely studied in the literature for structural vibration suppression purposes. Building on some analytical and experimental studies, the device has been modelled as an inerter in parallel with a nonlinear dashpot, the latter incorporating the fluid damping effects due to pressure drops. This simplified model is appropriate in the preliminary sizing and optimisation of the device design for earthquake engineering applications.

Based on this idealised model, two novel structural control schemes based on the fluid inerter have been proposed for improving the earthquake resilience of BI buildings. These strategies exploit the mass amplification effect and the damping properties of the fluid inerter to enhance the seismic performance of TMD systems. Considering the random nature of the earthquake excitation, the optimised parameters of the fluid inerter have been preliminarily identified via the stochastic dynamic analysis of the system, by incorporating the nonlinear behaviour of the device through the statistical linearization technique.

The seismic performance of the proposed structural control schemes based on the fluid inerter has been assessed via nonlinear RHA, considering a five-story BI building. To incorporate a realistic earthquake input, an ensemble of 44 historically recorded ground motions have been assumed as base acceleration, which fully accounts for the record-to-record variability and for the non-stationary character of actual seismic events. Excellent seismic performance of the proposed schemes has been observed, with reductions of displacements and of absolute floor accelerations of nearly 40-45% with regard to MAX values, and around 50% with regard to RMS values.

Finally, an ad-hoc approach to design the fluid inerter in such a way as to achieve the targeted values of inertance and nonlinear damping resulting from the optimisation procedure has been discussed. This approach is not trivial as the inertance and damping are coupled characteristics in a real fluid inerter. Some simple considerations and practical design guidelines simplify the procedure to convert the optimised fluid inerter parameters into actual device dimensions with just two free geometrical parameters among a larger set of unknowns.

Future work will deal with shake table testing of the proposed structural control schemes implemented on a 1:5 scale model for an appropriate validation of the numerical investigation carried out in this paper.

Acknowledgements

With regard to the experimental data, the contribution of N.D. Smith and all the technical support staff from the Department of Mechanical Engineering of the University of Sheffield is gratefully acknowledged. The second author PD would also like to acknowledge support of the Indonesia Endowment Fund For Education (LPDP).

References

[1] Smith, MC., (2002), Synthesis of mechanical networks: the inerter. IEEE Transactions on Automatic Control, **47**(10), 1648-1662.
[2] Smith MC, Wang FC. Performance benefits in passive vehicle suspensions employing inerters. Vehicle System Dynamics 2004; 42(4): 235-257.
[3] Chen MZQ, Papageorgiou C, Scheibe F, Wang F-C, Smith MC. The missing mechanical circuit. IEEE Circ Syst Mag 2009; 1531-636X:10-26.
[4] Scheibe F, Smith MC. Analytical solutions for optimal ride comfort and tyre grip for passive vehicle suspensions. Vehicle System Dynamics 2009; 47(10): 1229-1252.
[5] Shen Y, Chen L, Yang X, Shi D, Yang J. Improved design of dynamic vibration absorber by using the inerter and its application in vehicle suspension. J Sound Vib 2016; 361: 148-158.
[6] Hu Y, Chen MZ, Sun Y. Comfort-oriented vehicle suspension design with skyhook inerter configuration. J Sound Vib 2017; 405: 34-47.
[7] Evangelou S, Limebeer DJ, Sharp RS, Smith MC. Mechanical steering compensators for high-performance motorcycles. J Appl Mech 2007; 74(2): 332-346.
[8] Wang FC, Liao MK, Liao BH, Su WJ, Chan HA. The performance improvements of train suspension systems with mechanical networks employing inerters. Vehicle System Dynamics 2009; 47(7): 805-830.
[9] Jiang JZ, Matamoros-Sanchez AZ, Goodall RM, Smith MC. Passive suspensions incorporating inerters for railway vehicles. Vehicle System Dynamics 2012; 50(sup1): 263-276.
[10] Wang FC, Hsieh MR, Chen HJ. Stability and performance analysis of a full-train system with inerters. Vehicle System Dynamics 2012; 50(4): 545-571.
[11] Luo H, Zhang R, Weng D. Mitigation of liquid sloshing in storage tanks by using a hybrid control method. Soil Dyn Earth Eng 2016; 90: 183-195.
[12] Wang FC, Wu SY. Vibration control of an optical table employing mechatronic inerter networks. J Vib Control 2016; 22(1): 224-234.
[13] Li Y, Jiang JZ, Neild S. Inerter-based configurations for main-landing-gear shimmy suppression. Journal of Aircraft 2016; 54(2): 684-693.
[14] Makris N, Kampas G. Seismic protection of structures with supplemental rotational inertia. J of Eng Mech 2016; 142(11):04016089-1-11.
[15] Wang M, Sun F. Displacement reduction effect and simplified evaluation method for SDOF systems using a clutching inerter damper. Earth Eng Struct Dyn 2018; 1–22. https://doi.org/10.1002/eqe.3034.
[16] Marian L, Giaralis A. Optimal design of a novel tuned mass-damper-inerter (TMDI) passive vibration control configuration for stochastically support-excited structural systems. Prob Eng Mech 2014; 38, 156-164.
[17] Pietrosanti, D., De Angelis, M., Basili, M., (2017), Optimal design and performance evaluation of systems with Tuned Mass Damper Inerter (TMDI), Earthq Eng Struct Dyn 2017; 46(8): 1367-1388.

[18] Giaralis A, Taflanidis AA. Optimal tuned mass-damper-inerter (TMDI) design for seismically excited MDOF structures with model uncertainties based on reliability criteria. Struct Control Health Monit 2018; 25(2): e2082.
[19] De Domenico D, Ricciardi G. An enhanced base isolation system equipped with optimal Tuned Mass Damper Inerter (TMDI). Earthq Eng Struct Dyn 2018; 47: 1169-1192.
[20] Lazar IF, Neild SA, Wagg DJ. Using an inerter-based device for structural vibration suppression. Earthq Eng Struct Dyn 2014; 43: 1129-1147.
[21] Lazar IF, Neild SA, Wagg DJ. Vibration suppression of cables using tuned inerter dampers. Eng Struct 2016; 122: 62-71.
[22] Wen Y, Chen Z, Hua X. Design and Evaluation of Tuned Inerter-Based Dampers for the Seismic Control of MDOF Structures. J Struct Eng (ASCE) 2016; 143(4): 04016207.
[23] Sun L, Hong D, Chen L. Cables interconnected with tuned inerter damper for vibration mitigation. Eng Struct 2017; 151: 57-67.
[24] De Domenico D, Impollonia N, Ricciardi G. Soil-dependent optimum design of a new passive vibration control system combining seismic base isolation with tuned inerter damper. Soil Dyn Earth Eng 2018; 105:37-53.
[25] Papageorgiou C, Houghton NE, Smith MC. Experimental testing and analysis of inerter devices. J Dynam Syst Measurement Control 2008; 131(1): 011001.
[26] Gonzalez-Buelga A, Clare LR, Neild SA, Jiang JZ, Inman DJ. An electromagnetic inerter-based vibration suppression device. Smart Materials and Structures 2015; 24(5): 055015.
[27] Swift SJ, Smith MC, Glover AR, Papageorgiou C, Gartner B, Houghton NE. Design and modelling of a fluid inerter. Int J Control 2013; 86(11): 2035-2051.
[28] Glover AR, Smith MC, Houghton NE, Long PJG. Force-controlling hydraulic device (International Patent Application No: PCT/GB2010/001491, 2009).
[29] Gartner B, Smith MC. Damping and inertial hydraulic device (International Patent Application No: PCT/GB2011/000160, 2010).
[30] Flower WC. Understanding hydraulic mounts for improved vehicle noise, vibration and ride qualities, SAE Technical Paper 1 1985; 850975.
[31] Flannelly WG. Dynamic antiresonant vibration isolator, uS Patent 3,322,379, May 30 1967.
[32] Singh R. Dynamic design of automotive systems: Engine mounts and structural joints, Sadhana 2000; 25(3): 319-330.
[33] Golnaraghi MF, Nakhaie Jazar G. Development and analysis of a simplified nonlinear model of a hydraulic engine mount, J Vib Control 2001; 7(4): 495-526.
[34] Soltani P, Pinna C, Wagg DJ, Whear R. Ageing simulation of a hydraulic engine mount. Proc. IMechE, Part D: Journal of Automobile Engineering. DOI: 10.1177/0954407018786147.
[35] Ikago K, Saito K, Inoue N. Seismic control of single-degree-of-freedom structure using tuned viscous mass damper, Earthq Eng Struct Dyn 2012; 41(3): 453-474.
[36] Gonzalez-Buelga A, Lazar IF, Jiang JZ, Neild SA, Inman DJ. Assessing the effect of nonlinearities on the performance of a tuned inerter damper. Struct Control Health Monit 2017; 24(3): e1879.
[37] Shen Y, Chen L, Liu Y, Zhang X. Modeling and optimization of vehicle suspension employing a nonlinear fluid inerter. Shock and Vibration 2016; Article ID 2623017.
[38] Smith N, Wagg D. A fluid inerter with variable inertance properties. In: 6th European Conference on Structural Control (EACS2016), Sheffield, UK, 11-13 July 2016, paper no. 199.
[39] Shen Y, Chen L, Liu Y, Zhang X, Yang X. Optimized modeling and experiment test of a fluid inerter. Journal of Vibroengineering 2016; 18(5): 2789-2800.
[40] Shen Y, Chen L, Liu Y, Zhang X. Influence of fluid inerter nonlinearities on vehicle suspension performance. Advances in Mechanical Engineering 2017; 9(11): 1687814017737257.
[41] Liu X, Jiang JZ, Titurus B, Harrison A Model identification methodology for fluid-based inerters. Mechanical Systems and Signal Processing 2018; 106: 479-494.
[42] Deastra P, Wagg DJ, Sims ND. The realisation of an inerter-based system using fluid inerter. In Dynamics of Civil Structures, Volume 2 (pp. 127-134). Springer, Cham 2019.
[43] Deastra P, Wagg DJ, Sims ND. Modelling the hysteretic behaviour of a fluid inerter for use as a parallel-viscous-inerter-damper device. Proceedings of the 7WCSCM, Qingdao, China, 2018.

[44] Saito K, Yogo K, Sugimura Y, Nakaminami S, Park K. Application of rotary inertia to displacement reduction for vibration control system. 13th World Conference on Earthquake Engineering 2004; paper #1764, pp. 13.
[45] Takewaki I, Murakami S, Yoshitomi S, Tsuji M. Fundamental mechanism of earthquake response reduction in building structures with inertial dampers. Struct Control Health Monit 2012; 19:590-608.
[46] Saitoh M. On the performance of gyro-mass devices for displacement mitigation in base isolation systems. Struct Control Health Monit 2012; 19: 246-259.
[47] Hashimoto T, Fujita K, Tsuji M, Takewaki I. Innovative base-isolated building with large mass-ratio TMD at basement for greater earthquake resilience. Future Cities and Environment 2015;1:9: 1-19.
[48] Mirza Hessabi R, Mercan O. Investigations of the application of gyro-mass dampers with various types of supplemental dampers for vibration control of building structures. Eng Struct 2016; 126: 174-186.
[49] De Domenico D, Ricciardi G. Improving the dynamic performance of base-isolated structures via tuned mass damper and inerter devices: A comparative study. Struct Control Health Monit. 2018; 25(10), e2234. https://doi.org/10.1002/stc.2234.
[50] Ariga T, Kanno Y, Takewaki I. Resonant behaviour of base-isolated high-rise buildings under long-period ground motions. Structural Design of Tall and Special Buildings 2006; 15:325–338.
[51] Yang JN, Danielians A, Liu SC. Aseismic hybrid control systems for building structures. J Eng Mech 1991; 117: 836-853.
[52] Taniguchi T, Der Kiureghian A, Melkumyan M. Effect of tuned mass damper on displacement demand of base-isolated structures. Eng Struct 2008; 30:3478-3488.
[53] De Domenico D, Ricciardi G. Earthquake-resilient design of base isolated buildings with TMD at basement: Application to a case study. Soil Dyn Earth Eng 2018; 113: 503-521.
[54] De Domenico D, Ricciardi G. Optimal design and seismic performance of tuned mass damper inerter (TMDI) for structures with nonlinear base isolation systems. Earth Eng Struct Dyn 2018; 47: 2539-2560.
[55] De Domenico D, Ricciardi G, Benzoni G. Analytical and finite element investigation on the thermo-mechanical coupled response of friction isolators under bidirectional excitation. Soil Dyn Earthq Eng 2018; 106:131-147.
[56] De Domenico D, Falsone G, Ricciardi G. Improved response-spectrum analysis of base-isolated buildings: A substructure-based response spectrum method. Eng Struct 2018; 162: 198-212.
[57] Lu LY, Chen PR, Pong KW. Theory and experiment of an inertia-type vertical isolation system for seismic protection of equipment. J Sound Vib 2016; 366: 44-61.
[58] Masri SF, Caffrey JP. Transient response of a SDOF system with an inerter to nonstationary stochastic excitation. J Appl Mech 2017; 84(4): 041005.
[59] Masri SF, Caffrey JP, Li H. Transient Response of MDOF Systems With Inerters to Nonstationary Stochastic Excitation. J Appl Mech 2017; 84(10): 101003.
[60] Clough RW, Penzien J. Dynamics of Structures, 3rd ed. Berkeley, CA, USA: Computers and Structures Inc.; 2003.
[61] Der Kiureghian A, Neuenhofer A. Response spectrum method for multi-support seismic excitations. Earth Eng Struct Dyn 1992; 21: 713-740.
[62] Roberts JB, Spanos PD. Random Vibration and Statistical Linearization. New York: Wiley; 1990.
[63] De Domenico D, Ricciardi G. Improved stochastic linearization technique for structures with nonlinear viscous dampers. Soil Dyn Earth Eng 2018; 113: 415-419.
[64] Pan C, Zhang R, Luo H, Li C, Shen H. Demand- based optimal design of oscillator with parallel-layout viscous inerter damper. Struct Control Health Monit 2018; 25(1): e2051.
[65] Pan C, Zhang R. Design of structure with inerter system based on stochastic response mitigation ratio. Struct Control Health Monit 2018; 25(6): e2169.
[66] FEMA P695 (Federal Emergency Management Agency). Quantification of building seismic performance factors. Federal Emergency Management Agency, Washington, D.C.; 2009.
[67] Tributsch A, Adam C. Evaluation and analytical approximation of Tuned Mass Damper performance in an earthquake environment. Smart Structures and Systems 2012; 10(2): 155-179.